HOKKAIDO UNIVERSITY

Title	Interannual variability of precipitation over the Maritime Continent
Author(s)	Alsepan, Givo
Citation	. ( ) 14644
Issue Date	2021-09-24
DOI	10.14943/doctoral.k14644
Doc URL	http://hdl.handle.net/2115/87090
Type	theses (doctoral)
File Information	Givo_Alsepan.pdf

Instructions for use

Interannual variability of precipitation

over the Maritime Continent

(海洋大陸における降水の経年変動)

Thesis for a Doctorate

Givo Alsepan

ギヴォ　アルセパン

Department of Natural History Sciences, Graduate School of Science,

Hokkaido University

北海道大学大学院理学院　自然史科学専攻

September 2021

Abstract

Understanding the relationship between El Niño and the interannual climate variability over the Maritime Continent (MC) region has important socio-economic implications. Given that El Niño has tremendous impacts, studying how it affects the precipitation would create better awareness and preparedness for the potential effects when El Niño is predicted. This thesis describes a comprehensive understanding of the role of El Niño to precipitation variability by analyzing a high-resolution gauge-based precipitation dataset as well as the role of local and remote sea surface temperature (SST) anomalies during the El Niño events to the precipitation through numerical experiments.

Regional-scale precipitation responses over Indonesia, a region occupying almost 70% of the MC, to major climate modes in the tropical Indo–Pacific Oceans, namely, canonical El Niño, El Niño Modoki, and the Indian Ocean Dipole (IOD), and how the responses are related to large-scale moisture convergences are investigated. The precipitation responses, analyzed using a high-spatial-resolution (0.5° × 0.5°) terrestrial precipitation dataset for the period 1960–2007, exhibit differences between the dry (July–September) and wet (November–April) seasons. Canonical El Niño strongly reduces precipitation in central to eastern Indonesia from the dry season to the early wet season and northern Indonesia in the wet season. El Niño Modoki also reduces precipitation in central to eastern Indonesia during the dry season, but conversely increases precipitation in western Indonesia in the wet season. Moisture flux analysis indicates that corresponding to the dry (wet) season precipitation reduction due to the canonical El Niño and El Niño Modoki anomalous divergence occurs around the southern (northern) edge of the convergence zone when one of the two edges is located near the equator (10°S–15°N) associated with their seasonal migration. This largely explains the seasonality and

regionality of precipitation responses to canonical El Niño and El Niño Modoki. IOD reduces precipitation in southwestern Indonesia in the dry season, associated with anomalous moisture flux divergence. The seasonality of precipitation response to IOD is likely to be controlled by the seasonality of local sea surface temperature anomalies in the eastern pole of the IOD.

The contribution of remote and local SST forcing during El Niño in shaping the interannual variations of large-scale precipitation over the MC during July-October (JASO) and January-April (JFMA) seasons is investigated by using an atmospheric general circulation model (AGCM). Two idealized AGCM experiments are designed to isolate the effect of anomalous SST forcing from the tropical central-eastern Pacific (CEP) and tropical western Pacific (WP). In the first (second) experiment, the climatological SST field is specified in the tropical CEP (WP), while observed SST is specified elsewhere. Our numerical experiments indicate that, in the JASO season, the precipitation reduction over the southern hemisphere (SH) side of MC is likely explained as a direct influence of El Niño. In response to El Niño-related positive SST anomalies over the tropical CEP, twin Rossby wave cyclonic anomalies are generated to the tropical WP. The southern branch of the twin cyclonic anomalies advects dry air into the SH side of MC, which then suppresses convection and precipitation there. In the JFMA season, the reduced precipitation over the northern hemisphere (NH) side of MC is likely induced by the in-situ ocean surface cooling. The local cooling forcing promotes the generation of the Philippine Sea anticyclonic anomalies in the NH region. The eastern flank of the anomalous anticyclone transfers dry air into the NH side of MC and then reduces local precipitation.

Table of Contents

Chapter 1

General Introduction

On the interannual timescale, El Niño, which was initially translated from Spanish as 'the boy-child', is the dominant mode arising from the atmosphere and ocean interaction in the tropical Pacific (Wallace et al. 1998; Trenberth et al. 1998). During a normal condition, trade winds blow from east to west across the surface of the tropical Pacific Ocean, carrying warm moist air and warmer surface water towards the tropical western Pacific (WP) and keeping the tropical central-eastern Pacific (CEP) relatively cool. The warm sea surface temperature (SST) in the tropical WP pumps heat and moisture to the atmosphere above and favors the atmospheric convection, causing towering cumulonimbus clouds and rains. This now-drier air then travels eastward in the upper-troposphere before descending over the cooler CEP SST. The air rising in the west and falling in the east along with the westward-moving air at the surface is referred to as the Walker Circulation (Walker 1923, 1924). During El Niño, the trade winds weaken or even reverse, allowing the warmer water to move into the tropical CEP regions. Hence, the El Niño events are best-known as the occurrence of a strong SST warming in the tropical CEP and an eastward shift of the Walker circulation (Bjerkness 1969).

El Niño occurs every few years (say, two to seven years) and exhibits a great influence on the global climate (Webster et al. 1998). In general, it is strongly phase-locked to the annual cycle, developing in the boreal summer to autumn, peaking in winter, and decaying rapidly in the following spring (Rasmusson and Carpenter 1982; Deser et al. 2010). El Niños do not affect all regions over the globe, and even in a given area, the impacts are not exactly the same. Tropical climate variabilities associated with El Niño include drought in northern South America, higher than normal precipitation in

eastern equatorial Africa, and lower than normal conditions in Australia and Indian monsoon rainfall (Ropelewski and Halpert 1987). Within the tropical Pacific, a decrease in precipitation is large in the western Pacific and the Maritime Continent (MC) region (Quinn et al. 1978).

Given that the MC is a focal point of the climate mode influences, El Niño can bring some serious problems. It exerts impacts on human life and economic growth through modulating crop yields (Iizumi et al. 2014), severe droughts (Dai et al. 1998), and raging forest fires (Burton et al. 2020). According to the Food and Agriculture Organization (FAO) report released in March 2016, about 20 million USD has been provided to compensate for the impacts of a single El Niño event in 2015/16, including more than 50% crop failures and forest losses due to wildfires faced by many countries in the MC sector. Thus, understanding how El Niño influences the precipitation over the MC would be very beneficial for the scientific community as well as policymakers.

Indonesia occupies almost 70% of the MC, a region whose climate variability is modulated predominantly by the El Niño event. This climate mode tends to decrease Indonesian precipitation significantly from the boreal summer to winter and causes a longer than the normal dry season (Philander 1983a; Ropelewski and Halpert 1987; Hendon 2003; As-syakur et al. 2014; Yanto et al. 2016). Considering that El Niño can last up to 1 or 2 years, it is necessary to understand the seasonal evolution of El Niño influences to regional-scale Indonesian precipitation patterns. Furthermore, because the Indonesian climate is strongly characterized by the annual cycle of the convergence zones, such as the intertropical convergence zone (ITCZ) and the South Pacific convergence zone (SPCZ), it is also important to know how the seasonality of the convergence zones can modulate the seasonality of El Niño influences on precipitation. In chapter 2, we analyze

comprehensively the seasonal development of interannual variability of regional-scale Indonesian precipitation related to El Nino and other tropical Indo-Pacific climate modes, e.g., Indian Ocean Dipole (Saji et al. 1999) and El Niño Modoki (Ashok et al. 2007), including their relations with the convergence zones' behavior.

In the presence of positive SST anomalies in the tropical CEP during the El Niño events, negative SST anomalies are also generated in the tropical WP around the warm pool region (Wallace et al. 1998; Wu et al. 2017a). It is widely agreed that the positive SST anomalies exert significant global impacts, suggesting a potential remote influence on the MC's climate. However, it is also important to know whether the negative SST anomalies can have a direct influence on the local precipitation over the MC region because any variations of SST in the warm pool region can induce changes in the atmospheric circulations (Palmer and Owen 1986; Ju and Slingo 1995). One of the most obvious ways to understand the role of this local and remote SST anomaly is by using an atmospheric general circulation model (AGCM), which allows us to separate the forcing of the observed regional SST appropriately. In chapter 3, we use the AGCM For the Earth Simulator (AFES) developed by the Japan Agency for Marine-Earth Science and Technology (JAMSTEC) to investigate the relative contribution of local versus remote SST anomaly forcing in shaping the interannual variations of precipitation over the Maritime Continent during the El Niño events.

Chapter 2

Relations between interannual variability of regional-scale Indonesian precipitation and large-scale climate modes during 1960–2007

2.1. Introduction

Indonesia consists of more than 16 000 islands between the Pacific and Indian Oceans and between the Asian and Australian continents, and the main islands are mostly mountainous (Fig. 2.1). The seasonal evolution of the Indonesian climate is strongly influenced by the Asian–Australian monsoon systems (Qian et al. 2002; Hung et al. 2004) and is characterized by a wet season from November to April and a dry season from July to September (Fig. 2.2a). Climate variations, especially precipitation anomalies, can cause severe socioeconomic problems; crop failure occurs frequently during dry events (Amien et al. 1999; Naylor et al. 2001; D'Arrigo and Wilson 2008) as well as forest and peat fires (Siegert et al. 2001; Page et al. 2002; Waple and Lawrimore 2003; Pan et al. 2018), whereas heavier than normal precipitation can cause floods (Whetton and Rutherfurd 1994; Lawrimore et al. 2001; D'Arrigo et al. 2008). For example, extreme drought and the prolonged dry season in 2015 caused severe forest fires in western Indonesia, which contributed to large amounts of carbon emissions and forest losses (Huijnen et al. 2016; Noojipady et al. 2017; Pan et al. 2018). Therefore, better understanding of precipitation variability on a regional scale over the Indonesian region is important.

Indonesian precipitation variability is influenced by climate variability in the Pacific and Indian Oceans. Climate phenomena influencing Indonesian precipitation include El Niño–Southern Oscillation (ENSO), El Niño Modoki (Ashok et al. 2007), and

the Indian Ocean Dipole (IOD) (Saji et al. 1999). Previous studies have provided overviews of how these climate modes influence Indonesian precipitation. Canonical El Niño tends to reduce Indonesian precipitation between the boreal summer and winter (from the dry season to the wet season) and can cause a longer-than-normal dry season (Philander 1983a; Ropelewski and Halpert 1987; Philander 1990; Gutman et al. 2000; Hendon 2003). Ashok et al. (2007) found that El Niño Modoki has a similar impact in the dry season. A positive IOD, accompanied by negative sea surface temperature (SST) anomalies in the eastern tropical Indian Ocean, also decreases precipitation over Indonesia (Saji and Yamagata 2003; Ashok et al. 2004; Saji et al. 2006; Hamada et al. 2012; Nur'utami and Hidayat 2016; Lestari et al. 2018). These studies used the precipitation datasets of the Global Precipitation Climatology Project (GPCC; Adler et al. 2003) or Climate Prediction Center Merged Analysis of Precipitation (Xie and Arkin 1997) on a 2.5° × 2.5° grid, which are too coarse to investigate the regional-scale precipitation in Indonesia.

The relationship between regional Indonesian precipitation and climate modes has been recently investigated. As-syakur et al. (2014) analyzed the correlations between the precipitation over Indonesia and the El Niño index or Indian Ocean dipole mode index (IODMI) using a high-resolution (0.25° × 0.25°) satellite-derived precipitation dataset. They found that the effects of climate modes are not spatially stationary but exhibit seasonal migration. However, the analysis period of their study was relatively short (13 years, from 1998 to 2010), and hence it is unclear whether the regional patterns are robust over a longer period. Using high-resolution (0.5° × 0.5°) precipitation data from the University of East Anglia Climatic Research Unit (UEA-CRU) (Harris et al. 2014), Yanto et al. (2016) investigated the seasonally averaged precipitation variability in wet

(November–April) and dry (May–October) seasons over Indonesia, and analyzed their relationships with ENSO and Pacific decadal oscillation (Mantua et al. 1997), but they did not examine the seasonal evolution of the effects of climate modes. Furthermore, these high-resolution studies did not investigate the effects of El Niño Modoki [and also IOD for Yanto et al. (2016)], which are expected to be important in Indonesian precipitation variability (Ashok et al. 2007).

The purpose of this study is twofold. First, we clarify the seasonal development of regional precipitation responses over the Indonesian region to the climate modes in the Indo–Pacific Oceans, namely, ENSO, El Niño Modoki, and IOD, including the seasonal evolution of their influence. To this end, we analyze a recent, high-resolution (0.5° × 0.5°) terrestrial precipitation dataset, the Asian Precipitation–Highly Resolved Observational Data Integration Toward Evaluation (APHRODITE) (Yatagai et al. 2012), which covers 48 years, from 1960 to 2007. Second, we examine how the regional precipitation responses to climate modes are related to moisture flux divergence by analyzing a reanalysis dataset. In particular, we focus on how variations in Indonesian precipitation are related to convergence zones, such as the intertropical convergence zone (ITCZ) and South Pacific convergence zone (SPCZ) in the western Pacific Ocean (Vincent 1994) and the oceanic tropical convergence zone (OTCZ) over the equatorial Indian Ocean (Saji et al. 1999).

These convergence zones vary with respect to the variability of the Indo–Pacific climate modes. Canonical El Niño induces the eastward (northeastward) shifts of the ITCZ (SPCZ) in the equatorial Pacific Ocean, leading to divergences in the warm pool regions (Vincent 1994; Matthews and Kiladis 1999; Folland et al. 2002; Matthews 2012). During El Niño Modoki, the convergence zone migrations are similar to those during canonical El Niño (Weng et al. 2007, 2009). Freitas et al. (2017) showed northward

extreme shifts of the OTCZ over the southern Maritime Continent during IOD events. However, the relationship between the variability of convergence zones and regional-scale precipitation anomalies over Indonesia has not been examined. Furthermore, because transitions between dry and rainy seasons are closely related to the seasonal migration of convergence zones, it is important to understand how the seasonal migration modulates interannual variability of convergence zones and their influences on regional-scale precipitation variability.

2.2. Data and methods

We used the monthly APHRODITE data (Yatagai et al. 2012) from January 1960 to December 2007 with a horizontal resolution of 0.5° × 0.5° spanning from 93° to 143°E and from 11°S to 7°N (Fig. 2.1), which is narrower than the original dataset covering the Asian region. APHRODITE is a project that produces gridded precipitation dataset on a high-resolution grid based on rain gauge data over land (Yatagai et al. 2009, 2012). APHRODITE used the following data: Global Telecommunication System (GTS)-based data (global summary of the day) from the World Meteorological Organization; data precompiled by different groups or organizations; and raw observational data collected by the APHRODITE project. These incorporated data are 2.3–4.5 times greater than the number of GTS-only data and make the largest number of records in Indonesia, especially over southern regions (Yatagai et al. 2012), compared to other datasets with the same resolution, such as the UEA-CRU, University of Delaware, and GPCC (Schneider et al. 2008). APHRODITE uses careful gridding interpolation method by taking into account the mountains, ridges, and slopes (Schaake 2004), which should help to represent precipitation over the mountainous Indonesian area appropriately (Fig. 2.1). All data

were also subjected to thorough quality control procedures manually and automatically, which at least may avoid the abnormality of the data as found in the GPCC product where in September 2004 Indonesian precipitation reaches ~10 000 mm month^{-1} (Hamada et al. 2011; Yatagai et al. 2012). Recent studies have demonstrated the usefulness of APHRODITE products to improve seasonal forecasts of Asian monsoon precipitation (Yatagai et al. 2014), to validate high-resolution climate model simulations (Yatagai et al. 2005), and to characterize regional features of extreme precipitation in Southeast Asia (Villafuerte and Matsumoto 2015).

To understand the role of large-scale atmospheric circulation in precipitation variability over Indonesia, we also use the Japanese 55-Year Reanalysis (JRA-55) dataset (Kobayashi et al. 2015; Harada et al. 2016) with a 1.25° × 1.25° longitude and latitude grid for the same period as the APHRODITE data. By using the JRA-55 data, we estimate the vertically integrated moisture flux convergence between 1000 and 500 hPa based on monthly horizontal wind speed and specific humidity data, using the following equation:

$$-\mathbf{\nabla} \cdot \mathbf{Q} = \frac{1}{g} \int_{p_1}^{p_0} \left(\frac{\partial uq}{\partial x} + \frac{\partial vq}{\partial y} \right) dp, \qquad (2.1)$$

where $\mathbf{Q}$ represents the vertically integrated moisture flux, $-\mathbf{\nabla} \cdot \mathbf{Q}$ is its convergence, x and y are the zonal meridional coordinates, u and v are the x and y components of the horizontal wind, respectively, q is the specific humidity, p is the pressure, g is the gravitational acceleration, and the interval of vertical integration is between p_0 (1000 hPa) and p_1 (500 hPa). To examine the robustness of the analyses of moisture flux convergence, we also examined the NCEP–NCAR reanalysis dataset (Kalnay et al. 1996). The results of NCEP–NCAR reanalysis essentially confirm those of JRA-55.

To understand the relations between Indonesian precipitation anomalies and climate modes, we use three SST-based climate indices: the Niño-3 index, El Niño Modoki

12

index (EMI), and IODMI. These indices are calculated using the monthly, $1° \times 1°$ grid SST dataset of the Hadley Centre Sea Ice and Sea Surface Temperature version 1.1 (HadISST1.1) data (Rayner et al. 2003). The Niño-3 index is the area-averaged SST anomaly (SSTA) over the region of 150°–90°W, 5°S–5°N. The EMI (Ashok et al. 2007) is defined as $[SSTA]_{CP} - 0.5 \times [SSTA]_{EP} - 0.5 \times [SSTA]_{WP}$, where the square brackets represent the area-averaged SSTA over the central Pacific (CP; 165°E–140°W, 10°S–10°N), eastern Pacific (EP; 110°–70°W, 15°S–5°N), and western Pacific (WP; 125°–145°E, 10°S–20°S). The IODMI (Saji et al. 1999) is the SSTA difference between the western (50°–70°E, 10°S–10°N) and southeastern (90°–110°E, 10°S–0°) Indian Ocean. The relations between the climate modes and Indonesian precipitation variability are investigated using standard correlation (or Pearson correlation) analysis and partial correlation analysis of the annually sampled 3-month average data between the precipitation and the respective climate indices for each calendar month. For simplicity, the 3-month average is denoted as the value of the center month; for example, December–February (DJF) is denoted as January, unless otherwise stated. Because climate indices are not independent, the partial correlation analysis is used to access the independent contributions of climate indices to precipitation variability. A partial correlation technique has been used to study the impacts of El Niño and IOD (Ashok and Saji 2007; Cai et al. 2009; As-syakur et al. 2014) and El Niño Modoki (Ashok et al. 2007). It is noteworthy that to judge whether standard or partial correlation is more appropriate, a priori knowledge is required. For example, if the influences of climate indices A and B on variable C are analyzed, and if there is a priori knowledge that climate index A drives index B and not vice versa, then it is appropriate to use standard correlations for index A with variable C and partial correlations for index B. However, such a priori knowledge is

not generally available, and the partial correlation gives a conservative measure as a correlation that holds even if the other climate indices drive the climate index in question. Please note that, in this paper, anomalies of all variables are defined as the deviations from the mean seasonal climatology (from January 1971 to December 2000), and the linear trends of anomalies are removed.

2.3. Basic features of Indonesian precipitation

Before examining the relationship between Indonesian precipitation and climate indices, we briefly describe the basic features of Indonesian precipitation, including the seasonal march, which is strongly controlled by the Asian–Australian monsoon (Haylock and McBride 2001; Aldrian and Susanto 2003). Figure 2.2a shows that area-averaged climatological terrestrial precipitation reaches its minimum in August and maximum in December. The narrow trough and wide peak mean the short dry season (July–September) and long wet season (November–April) accompanied by the rapid dry-to-wet transition in October and slow wet-to-dry transition from May to June. The spatial map of climatological mean precipitation in the dry season and wet season (Figs. 2.2b,c) indicates that the difference between high and low precipitation is large not only between the two seasons, but also among different regions. In the dry season, precipitation is especially low in southern Indonesia (Java and Nusa Tenggara) and relatively low in central to eastern Indonesia (Sulawesi and Maluku). In contrast, in the wet season, precipitation is high over Java and central Borneo. These regional differences in the seasonal marches are important in understanding the effects of precipitation anomalies; anomalously low (high) precipitation in the regions of climatologically low (high) precipitation can cause severe problems in the dry (wet) season.

2.4. Overall influence of climate modes

To measure the contribution of the climate modes to Indonesian precipitation variability, we calculate the explained variance ratios of Indonesian precipitation by the SST-based climate indices (Fig. 2.3). The explained variance ratio is defined as the variance of the estimated component based on a linear regression divided by the total variance. The explained variances of all climate modes are generally large between the dry season and early wet season (July–November), and reach their respective peaks in September. If 10% of explained variance is used as a threshold of substantial contribution, canonical ENSO has the largest number of months of substantial contributions from July to January, that is, from the dry season through the first half of the season. In most of these months, the canonical ENSO makes the largest contribution to precipitation variability compared with other modes. The IOD contribution is higher than 10% from July to November, and slightly exceeds that of canonical ENSO in September and October. The contribution of El Niño Modoki exceeds 10% from August to November and is smaller than the canonical El Niño and IOD contributions in those months.

A caveat of the explained variances is that the climate modes are not independent. Thus, a certain portion of the explained variance of one climate mode may not reflect direct causality, and the variance can contain contributions from other modes. To measure the magnitude of the mode interactions, we examine correlation coefficients among the climate indices (Fig. 2.4). Relatively strong correlation (>0.5) occurs between canonical El Niño and IOD from September to November consistent with Ashok et al. (2003a), overlapping the period when the explained variances of these modes are generally large. The square of the correlation gives a measure of the mode interaction for variances. For example, in September, when the explained variances of all climate modes are the highest,

15

the correlation between canonical El Niño and IOD is 0.55, which means that 30% of variance of canonical El Niño or IOD can be contributed by the other climate mode. Because it is not possible to distinguish which climate mode forces which, we examine both standard correlation and partial correlation for relations between precipitation and climate modes in the next section.

2.5. Role of the climate modes with regard to precipitation

2.5.1. Canonical El Niño

Figure 2.5 shows the seasonal evolution of correlations between precipitation and Niño-3 in each calendar month. Negative correlations cover a wide area over central to eastern Indonesia from July to November, namely, from the dry season to the early wet season, corresponding to the top five months of explained variances of Niño-3 (Fig. 2.3). Monthly evolution indicates that canonical El Niño first affects southern Borneo, Sulawesi, Maluku, and western Papua, and then its influence expands southward to Java and Nusa Tenggara. Lower precipitation in the dry season means that canonical El Niño can cause drought in central to eastern Indonesia. Subsequently, the negative correlations occur in a more limited area over northern Indonesia in the middle and late wet season. In the months, the negative correlations occur mainly over northern Borneo, northern Sulawesi, and northern Maluku. The distinct difference in correlation patterns between dry and middle-late wet seasons suggests that precipitation responses to canonical El Niño over Indonesia are caused by at least two mechanisms.

The different patterns of precipitation response to canonical El Niño in different seasons found by correlation analysis (Fig. 2.5) are generally confirmed by the partial correlations between precipitation and Niño-3 after removing the contributions of El Niño

16

Modoki and IOD (Fig. 2.6). The magnitudes of partial correlations are generally smaller than standard correlations, but still strong partial correlations are found in central–eastern Indonesia in the dry season and in northern Indonesia in the wet season. This means that the contrast between two seasons is not due to the mode interaction, but occurs intrinsically as the precipitation response to the canonical El Niño.

The influence of El Niño and La Niña events on precipitation in Indonesia is examined by comparing the time series of the Niño-3 index and area-averaged precipitation anomalies. The time series are chosen for central to eastern Indonesia between August and October from the dry season (Fig. 2.7a) and northern Indonesia between February and April from the wet season (Fig. 2.7b). In central to eastern Indonesia, the two time series are generally consistent throughout the analysis period, but in northern Indonesia there is a strong relationship apparent only after the 1980s, including a large precipitation reduction of more than two standard deviations for the 1982/83 and 1997/98 El Niños, known as extreme El Niños (Philander 1983b; McPhaden 1999). This change in relationship after 1980 may be associated with the 1970s climatic regime shift (Minobe 1997; Mantua et al. 1997). To examine if such a change of relationship occurs in other data than APHRODITE, we analyze station data, combining daily station data obtained from the Indonesian Meteorological, Climatological, and Geophysical Agency and monthly station data of Global Historical Climatology Network version 2. We need to combine the two datasets to obtain continuous monthly time series for the present analysis period (i.e., 1960–2007). There are three stations in northern Indonesia that have available data for the whole analysis period. They are Polonia in northern Sumatra, Tarakan in northern Borneo, and Manado in northern Sulawesi. Correlation coefficients between station precipitation and Niño-3 in March after (before)

17

the 1980s are 0.57 (0.32), 0.64 (0.01), and 0.79 (0.38) in Polonia, Tarakan, and Manado, respectively. Therefore, the weak and strong correlations roughly before and after the 1970s regime shift, respectively, are confirmed by the station data analysis.

To understand how the seasonal development of canonical El Niño influences is related to large-scale atmospheric fields, we conduct a partial correlation analysis between the convergence of the vertically integrated horizontal moisture flux and Niño-3 (Fig. 2.8). In both the dry and wet seasons, shown for September and March, respectively, the precipitation partial correlations in Fig. 2.6 are closely associated with moisture flux convergence partial correlations. The regions of precipitation partial correlations, central to eastern Indonesia in the dry season (July–September) and northern Indonesia in the wet season (November–April), are covered by the area of negative partial correlations of moisture flux convergence, corresponding to divergent anomalies. This means that the canonical El Niño reduces Indonesian precipitation on regional scales through larger-scale moisture divergence.

The negative partial correlations of moisture convergence in Fig. 2.8 generally occur around the climatological zero contours in both seasons, but their relations to ITCZ and SPCZ, which are somewhat merged over Indonesia, are different between the two seasons. In the dry season, negative partial correlations occur around the southern edge of the SPCZ, whereas they occur around the northern edge of the ITCZ in the wet season. This means that SPCZ (ITCZ) contracts northward (southward) in its southern (northern) flank in the dry (wet) season. Since the SPCZ and ITCZ are somewhat merged over Indonesia, zero contours occur only along the southern edge of the SPCZ and the northern edge of the ITCZ. Consequently, the rain reductions influenced by canonical El Niño over Indonesia are explained by the two different areas of divergent moisture flux anomalies;

one occurs in central to eastern Indonesia in the dry season, and the other occurs in the Philippine Sea and covers northern Indonesia in the wet season, associated with the northward contraction of the southern flank of the SPCZ and the southward contraction of the northern flank of the ITCZ, respectively. Next, we examine how the seasonality of the anomalous moisture flux divergence is related to the seasonal migration of convergence zones.

Figure 2.9 shows the seasonal evolution of the partial correlations between Niño-3 and moisture flux convergence zonally averaged between 110° and 150°E along with the climatologies of the convergence. The negative partial correlations corresponding to anomalous divergence occur between the equator and 10°S in the dry season and between the equator and 15°N in the wet season, consistent with Fig. 2.8. This feature can be explained if two conditions constrain the anomalous divergence in response to canonical El Niño. The anomalous moisture flux divergence occurs if the following two conditions are satisfied: 1) around the southern edges of the SPCZ or the northern edges of the ITCZ and 2) only in the latitudinal range between 10°S and 15°N. These conditions roughly constrain when and where the anomalous divergences occur, because they are satisfied only when the southern boundary of SPCZ comes within 10°S–0° or the northern boundary of ITCZ comes within 15°N–0°. The former occurs in the dry season in the Southern Hemisphere with moisture divergence anomalies occurring between 12°S and 3°N, whereas the latter occurs in the wet season in the Northern Hemisphere with moisture divergences occurring between 2° and 15°N (Fig. 2.9). Although these two conditions are observed features, we do not know what their underlying mechanisms are. Nevertheless, the interpretation combined with the spatial distribution of the moisture flux convergence anomalies shown in Fig. 2.8 can explain why precipitation reduction

19

occurs due to canonical El Niño in central to eastern Indonesia in the dry season and in northern Indonesia in the wet season, consistent with the precipitation anomalies shown in Fig. 2.5.

2.5.2. El Niño Modoki

In this subsection, we examine how El Niño Modoki influences precipitation in Indonesia. Figure 2.10 shows correlation coefficients between the EMI and precipitation. The correlations are negative in the dry season (July–September) and dry-to-wet transition (October) in central to eastern Indonesia and in the northern region in the middle of the wet season (January–March). In the wet season, however, a more salient feature is the positive correlations in western Indonesia, especially in Sumatra. The negative correlations for El Niño Modoki generally overlap with the negative correlation for canonical El Niño, whereas the positive correlations occur only for El Niño Modoki.

The partial correlations between the precipitation and EMI confirm that the relations found in correlations are contributed by El Niño Modoki (Fig. 2.11). In the dry season and dry-to-wet transition negative partial correlations occur in central to eastern Indonesia. Although in this region, partial correlations for canonical El Niño are also significant, as shown in section 2.5.1, there are subtle but interesting differences between El Niño Modoki and canonical El Niño. In the late dry season (September), El Niño Modoki has significant partial correlations in southern Indonesia (Nusa Tenggara) but canonical El Niño does not. In the dry-to-wet transition (October), El Niño Modoki has a stronger influence in central to eastern Indonesia than canonical El Niño. In the wet season, the positive partial correlations in western and central Indonesia, which are not seen for canonical El Niño, are consistent with those in standard correlations (Figs. 2.10 and 2.11). The negative correlations of precipitation over Indonesia for El Niño Modoki

were also reported by Ashok et al. (2007) using a coarse-resolution (2.5° × 2.5°) dataset, but our high-resolution (0.5° × 0.5°) analysis reveals the influence of El Niño Modoki in greater detail, including positive partial correlations in western and central Indonesia. The positive correlation in the wet season means that El Niño Modoki can bring floods in western Indonesia, contrary to the general expectation that El Niños cause drought in the Maritime Continent, including Indonesia.

To know better the relation between precipitation and El Niño Modoki for the increase in precipitation due to El Niño Modoki in western and central Indonesia, we plot time series of area-averaged precipitation anomalies and EMI in the wet season (Fig. 2.12). Close covariability is apparent between central Sumatra precipitation and the EMI in November (Fig. 2.12a), and between central Sumatra and southern Borneo precipitation and the EMI in March (Fig. 2.12b). Interestingly, the time scales for El Niño Modoki and corresponding precipitation are longer than those for canonical El Niño (Fig. 2.7), consistent with the fact that El Niño Modoki exhibits large decadal variability (Ashok et al. 2007; Weng et al. 2007).

Partial correlation analysis of moisture flux convergence with EMI shows two different areas of anomalous divergences in different seasons (Fig. 2.13), corresponding to the anomalous Indonesian precipitation during El Niño Modoki. The negative partial correlation of moisture flux convergence occurs in the dry season in central to eastern Indonesia. This negative partial correlation with El Niño Modoki is located slightly south of those with Niño-3 (Figs. 2.8a and 2.13a), which may explain the aforementioned stronger influence of El Niño Modoki on precipitation in southern Indonesia (Nusa Tenggara) compared with canonical El Niño (Figs. 2.6 and 2.11). Another negative partial correlation also occurs in the wet season (Fig. 2.13b) in the Philippine Sea, corresponding

to a brief precipitation reduction in northern Indonesia (Figs. 2.10 and 2.11). For the positive precipitation correlations with El Niño Modoki in western Indonesia, no corresponding significant correlations are found in the moisture flux convergence. Consequently, the precipitation decrease due to El Niño Modoki in central to eastern Indonesia in the dry season and northern Indonesia in the wet season can be explained by the anomalous moisture flux convergence, whereas the precipitation increase in the western region is not explained.

The zonally averaged partial correlation between EMI and moisture flux convergence along with the climatologies of the convergence (Fig. 2.14) indicates that the seasonality of the El Niño Modoki influence is related to the seasonal migration of convergence zones. Similar to the case of the canonical El Niño (Fig. 2.9), anomalous moisture flux divergence occurs when the edges of the convergence zones (zero climatology contours) are located near the equator between 10°S and 15°N (Fig. 2.14). However, there is an interesting difference: moisture flux divergence anomalies related to El Niño Modoki are more intense on the area of climatological divergence (Figs. 2.13 and 2.14) than those related to canonical El Niño (Figs. 2.8 and 2.9). Furthermore, in the dry-to-wet transition, anomalous divergences with El Niño Modoki are stronger than those with canonical El Niño (Figs. 2.9 and 2.14). This is consistent with the difference of precipitation responses; precipitation responses for El Niño Modoki compared with those for canonical El Niño in the dry (wet) season occur in more southern (northern) areas in central to eastern (northern) Indonesia (Figs. 2.6 and 2.11) and precipitation is more strongly reduced for El Niño Modoki than for canonical El Niño in the dry-to-wet transition.

2.5.3. IOD

Figure 2.15 shows that negative precipitation correlations with IODMI occur over a wide area of Indonesia from the dry season to the early wet season (July–November). In July, significant correlations cover the western–central parts, and then they increase their magnitudes until September with eastward expansion, followed by weakening in October and November. The pattern substantially overlaps with that of the correlations with Niño-3 (Fig. 2.5), and the strong correlation between Niño-3 and IODMI shown in Fig. 2.4 suggests that substantial parts of the correlations shown in Fig. 2.15 can come from the interaction between the impacts.

Partial correlations between the precipitation and IODMI (Fig. 2.16) are strong in southwestern Indonesia, especially in southern Sumatra and Java in the dry season (July–September) and dry-to-wet transition (October) and in central Indonesia (i.e., southern Borneo and Sulawesi), with weaker magnitudes. The highest absolute correlation reaches 0.7, much higher than that reported by As-syakur et al. (2014), which was lower than 0.4 (Fig. 3 in their paper). In these regions and seasons, partial correlations of IOD are much stronger than those of canonical El Niño or El Niño Modoki (Figs. 2.6 and 2.11), thereby indicating that the IOD is a dominant driver. This is consistent with the correlation analysis by Saji et al. (1999) and the partial correlation analysis by Ashok et al. (2007) (Fig. 9d in their paper). Our analysis using higher-resolution data than those used in previous studies not only confirms the robust relation between IOD and Indonesian precipitation in general, but also reveals the IOD's influence on Sulawesi, which was not found in earlier studies.

The precipitation time series of the regions influenced by IOD events in southwestern Indonesia negatively correlates with the IODMI in September (Fig. 2.17).

Although some mode interaction between IOD and canonical El Niño is expected (Fig. 2.4), these time series for IOD have different features from those for canonical El Niño. For example, the events of strong precipitation reduction in 1961, 1994, and 2006 are caused by the strong IOD events without canonical El Niños (Yamagata et al. 2004; Meyers et al. 2007; Vinayachandran et al. 2007). Moreover, the precipitation time series are not strongly affected by major El Niño events in 1972, 1982, and 1997, consistent with the weak influence of El Niño in southwestern Indonesia (Figs. 2.5 and 2.6).

The partial correlation between moisture flux convergence and the IODMI (Fig. 2.18) indicates that anomalous moisture flux divergences develop in June in the southeastern Indian Ocean and reach their peak in September, as shown for July and September (see also Fig. 2.19 for seasonal development). Negative partial correlations occur around the zero contour of the climatological moisture flux convergence, which is the southeastern edge of the OTCZ, and this indicates the northwestward contraction of the eastern OTCZ in the dry season. The spatial–seasonal distribution of anomalous divergences is consistent with the spatial pattern of the precipitation response to the IOD shown in Fig. 2.16. Therefore, the IOD reduces precipitation over southwestern Indonesia via the northward contraction of the OTCZ's southern boundary in the dry season and dry-to-wet transition.

The development of anomalous moisture flux divergence related to IOD probably has a different cause from those related to canonical El Niño and El Niño Modoki. For the latter climate modes, seasonal migration of the ITCZ and SPCZ plays an important role, as shown in section 2.5.1 and 2.5.2, but we find no relation between the seasonal OTCZ migration and the seasonal dependence of the anomalous moisture flux divergence in the eastern Indian Ocean. To understand what determines the seasonality of the IOD

24

influences on moisture flux convergence, we analyze the seasonal march of the SST anomalies in the eastern pole of the IOD (Fig. 2.19). Consistent with the seasonal development of the negative partial correlations between the moisture flux convergence and the IODMI, the strong negative partial correlations ($r < -0.7$) between the SST and IODMI start to develop in June, reach their peak in September, and then decline. This is consistent with the previously reported seasonal march of SST anomalies associated with IOD (Saji et al. 1999; Delman et al. 2018). This seasonality in the IOD's eastern pole is also consistent with the seasonality of the precipitation responses to the IOD (Fig. 2.16). Therefore, these results strongly suggest that seasonality of the precipitation response to IOD is controlled by the seasonality of the IOD itself.

2.6. Summary and discussion

We have investigated Indonesian precipitation responses to the three climate modes, namely, the canonical El Niño, El Niño Modoki, and IOD, for their regional and seasonal distribution and their relation to large-scale moisture flux convergence by using a high-resolution ($0.5° \times 0.5°$) terrestrial precipitation dataset APHRODITE (Yatagai et al. 2012) and JRA-55 reanalysis (Kobayashi et al. 2015) from January 1960 to December 2007. Although several studies have investigated precipitation in Indonesia related to climate modes using high-resolution data (see section 2.1), the present study provides a more comprehensive understanding of seasonally dependent regional-scale responses to climate modes and how regional-scale responses are related to the large-scale variability of the ITCZ and SPCZ.

Canonical El Niño and El Niño Modoki have some similarities. These two climate modes reduce precipitation in central and eastern Indonesia in the dry season

(July–September) and dry-to-wet transition (October), and in northern Indonesia in the wet season (November–April) (Figs. 2.5, 2.6, 2.10, and 2.11). Canonical El Niño has a stronger influence than El Niño Modoki in northern Indonesia in the wet season, but a weaker influence in central and eastern Indonesia in the dry-to-wet transition. The main features of these precipitation reductions can be explained by the large-scale moisture flux divergence. Anomalous moisture flux divergence occurs only when either the northern or southern edges of the merged convergence zone of ITCZ and SPCZ are located near the equator between 10°S and 15°N. This can occur in the dry or wet seasons when the southern or northern edge reaches this latitudinal range, respectively (Figs. 2.8, 2.9, 2.13, and 2.14). The anomalous divergences of moisture flux occur around the convergence zone edges for canonical El Niño, inducing convergence zone contractions. The anomalous divergences occur mainly on the area of climatological divergence for El Niño Modoki, namely, higher latitudes than for canonical El Niño. In addition, the dry-to-wet transition divergent anomalies are stronger for El Niño Modoki than for canonical El Niño. These differences in moisture flux divergence between the canonical El Niño and El Niño Modoki explain the differences in precipitation responses between the two modes. It is also found that El Niño Modoki increases precipitation in western Indonesia, contrary to the widely accepted view that El Niños decrease precipitation on the Maritime Continent. This precipitation increase cannot be explained by the moisture flux convergence.

The standard and partial correlation analyses indicate that IOD strongly influences southwestern Indonesia (southern Sumatra and Java) (Figs. 2.15 and 2.16). This large precipitation reduction is closely associated with anomalous divergences of the moisture flux in the equatorial eastern Indian Ocean over the southern flank of OTCZ

(Fig. 2.18), indicating the northward contraction of the OTCZ. The seasonality of the moisture flux divergence associated with the IOD is controlled by the seasonality of the SST anomalies of the IOD's eastern pole (Fig. 2.19).

The methods used in this study to identify the roles of climate modes in some regions also become a limitation owing to mode interactions, especially that between the IOD and canonical El Niño, which has relatively high correlations (Fig. 2.4). For example, strong negative correlations are found in southern Borneo both for canonical El Niño and the IOD in the dry season, accompanied by much weaker partial correlations for both modes. In this region and season, therefore, it is not possible to identify which of the two modes plays a dominant role in precipitation responses. Nevertheless, in most regions and seasons the results of the standard and partial correlations essentially the same. Consequently, the present results provide useful information for understanding of regional-scale Indonesian precipitation responses to climate modes in different seasons and how they are related to large-scale atmospheric conditions represented by convergence zones.

Although we have examined simultaneous correlations, lead–lag correlations might provide different patterns associated with development and decay years of canonical El Niño and El Niño Modoki. For instance, the ENSO-related Indian summer monsoon precipitation shows different patterns during the concurrent summer and following summer (Mishra et al. 2012). To examine this possibility, lead–lag partial correlations are calculated with respect to December Niño-3 and December EMI against precipitation with 3-month running average (figure not shown). December is taken as an index because it is usually the peak phase of ENSOs (Xie et al. 2009). The patterns of lead–lag partial correlations are, in general, qualitatively similar to those of simultaneous

partial correlations for the same calendar month of precipitation for lags of 3–4 months with smaller correlation values for the former than the latter. An exception is that partial correlations of March–April lagged to December Niño-3 are much weaker than simultaneous partial correlations. Please note that a 3-month period is the minimum lag so that the months in two time series are not overlapped in association with the 3-month running average. For leads or lags of 5 months or larger, lead–lag partial correlations become very small. Consequently, the simultaneous correlation analyses presented in this paper capture the main features of canonical El Niño and El Niño Modoki influences onto Indonesian precipitation.

It is also worth considering the influences of other tropical climate modes, such as basinwide warming in the tropical Indian Ocean (Kelin et al. 1999) and Atlantic Niño in the tropical Atlantic Ocean (Zebiak 1993). Previous studies suggested that the Indian Ocean basinwide (IOBW) mode has significant influences on climate anomalies over the Indo-western Pacific from boreal winter to the following summer (Yang et al. 2007; Xie et al. 2009). Atlantic Niño may affect the tropical Pacific variability (Rodríguez-Fonseca et al. 2009; Ding et al. 2012) and may modulate the regional climate variability such as in India in boreal summer (Kucharski et al. 2007). To investigate the influences of these climate modes, we calculate the partial correlation of Indonesian precipitation with the IOBW index and Atlantic Niño index for each calendar month by removing the influences of the two types of Pacific El Niño. The IOBW index (Atlantic Niño index) is defined as the area-averaged SST anomalies over the regions of 40°–100°E, 20°S–20°N (20°W–0°, 3°S–3°N). The partial correlations of precipitation with the two indices show that there are no significant values of correlation coefficients found over the Indonesian region in all seasons (figure not shown). This may indicate that both IOBW and Atlantic Niño have no

substantial influences to precipitation over Indonesia.

Further studies are necessary to understand the underlying mechanisms for anomalous moisture flux divergence and regional precipitations. For example, future studies are needed to explain why anomalous moisture flux divergence occurs around the convergence zone edges for canonical El Niño and El Niño Modoki and why the occurrences are limited between 10°S and 15°N. The distance from the equator for this sensitive response in on the order of the equatorial Rossby radius of deformation, and thus we speculate that dynamics, such as equatorial waves, may be important. In particular, Matsuno–Gill dynamics may play some role, as it is known that it is important in atmospheric response for El Niños and IODs (Ashok et al. 2003b; Guan et al. 2003; Lee et al. 2009; Ratnam et al. 2014). Numerical models should be useful for understanding the mechanisms. Probably large-scale convergence zone responses can be studied by global models (e.g., Preethi et al. 2015), but in order to understand the regional precipitation responses over mountainous Indonesian areas higher-resolution models than standard AGCMs are required. Along this direction, recent model intercomparison projects provide important research assets including regional model intercomparison of the Coordinated Regional Climate Downscaling Experiment (Ngo-Duc et al. 2017) and high-resolution global model intercomparison, the HighResMIP (Haarsma et al. 2016; Roberts et al. 2018).

The information obtained in this work may be useful to both the research community and society. Operational predictions using climate modes are conducted by a number of climate research centers over the world (e.g., Doi et al. 2016). Although the numerical model resolutions used for those predictions are not high enough to resolve the regional-scale precipitation variability, the climate mode predictions and the present

results can be combined to add values of these predictions. For example, if El Niño Modoki is predicted, central to eastern Indonesia should prepare for droughts, especially in the south, whereas western Indonesia should prepare for floods. Furthermore, the information of the present study can also be useful for determining how the influence of El Niño on Indonesian precipitation will change by future climate change. Previous studies have suggested that the frequency of El Niño Modoki events will increase due to global warming (Ashok et al. 2007; Ashok and Yamagata 2009; Yeh et al. 2009; Lee and McPhaden 2010), which may weaken the overall effects of El Niños on Indonesia because canonical El Niño has a stronger effect than El Niño Modoki. However, the change in type of El Niño may bring worse conditions in some regions, as shown by the different regionality between the canonical El Niño and El Niño Modoki. Hui and Zheng (2018) pointed out that IOD amplitudes in the eastern pole of the IOD will be enhanced in the future, thereby suggesting that the IOD may cause more severe effects on precipitation in southwestern Indonesia. To address the changes in relationships between climate modes and Indonesian precipitation, analyses of climate models, such as those in the Coupled Model Intercomparison Project, are necessary. For those studies, the present results can be used to know how future climate mode changes are related to Indonesian precipitation on finer scales that are not resolved by those models. Also, the present results can be used to know which climate models are appropriate for such studies, by judging whether the responses of large-scale convergence zones to climate modes are realistic in those models.
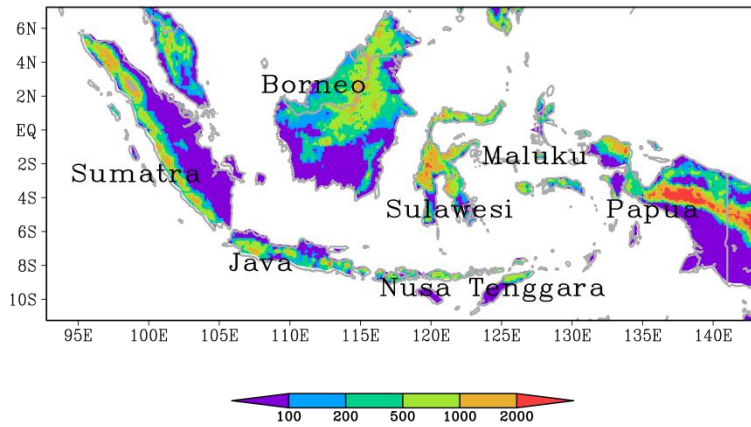
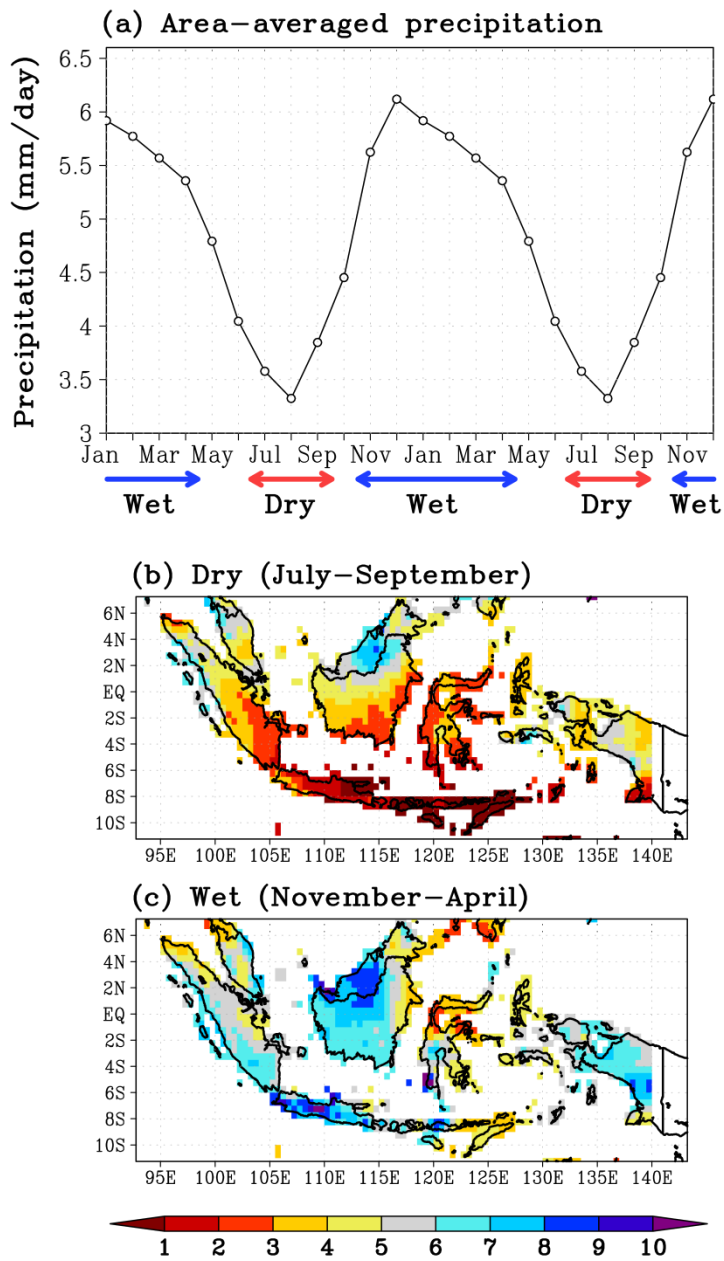Figure 2.1. Topography (m) of Indonesia in the study area based on the Worldbath dataset (http://ingrid.ldgo.columbia.edu/SOURCES/.WORLDBATH/.bath/).

(a) Area–averaged precipitation

(b) Dry (July–September)

(c) Wet (November–April)

Figure 2.2. (a) Monthly climatology (mm day⁻¹) of spatially averaged terrestrial precipitation over the area shown in Fig. 2.1. Seasonal climatology (mm day⁻¹) of precipitation in the (b) dry (July–September) and (c) wet (November–April) seasons for the period 1971–2000. Red and blue arrows indicate the dry and wet seasons, respectively.

32
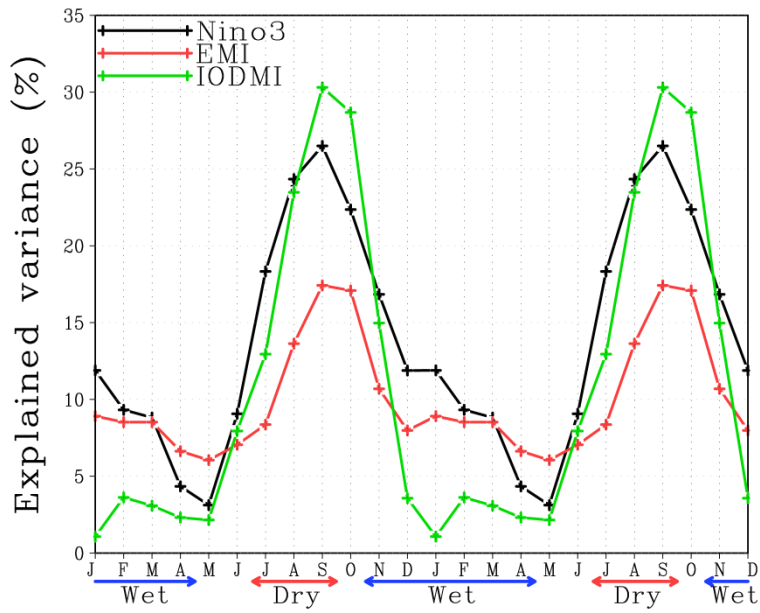
Figure 2.3. Explained variance ratio of Indonesian precipitation by SST-based climate indices with the 3-month average as a function of calendar month. Red and blue arrows indicate the dry and wet seasons, respectively. The x axis indicates the center of month of the 3-month average.
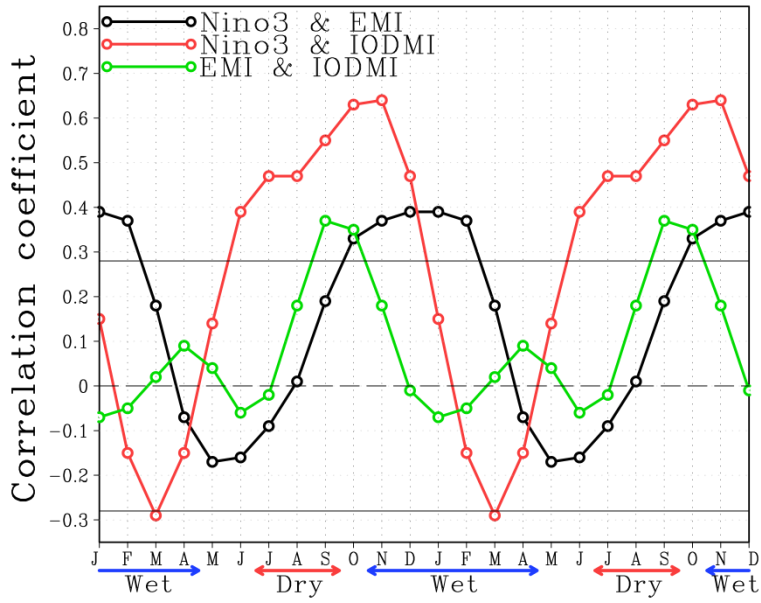
Figure 2.4. Correlation coefficients among SST-based climate indices with the 3-month average as a function of calendar month. The values outside the solid lines are statistically significant at the 95% confidence level. Red and blue arrows indicate the dry and wet seasons, respectively. The x axis indicates the center month of the 3-month average.
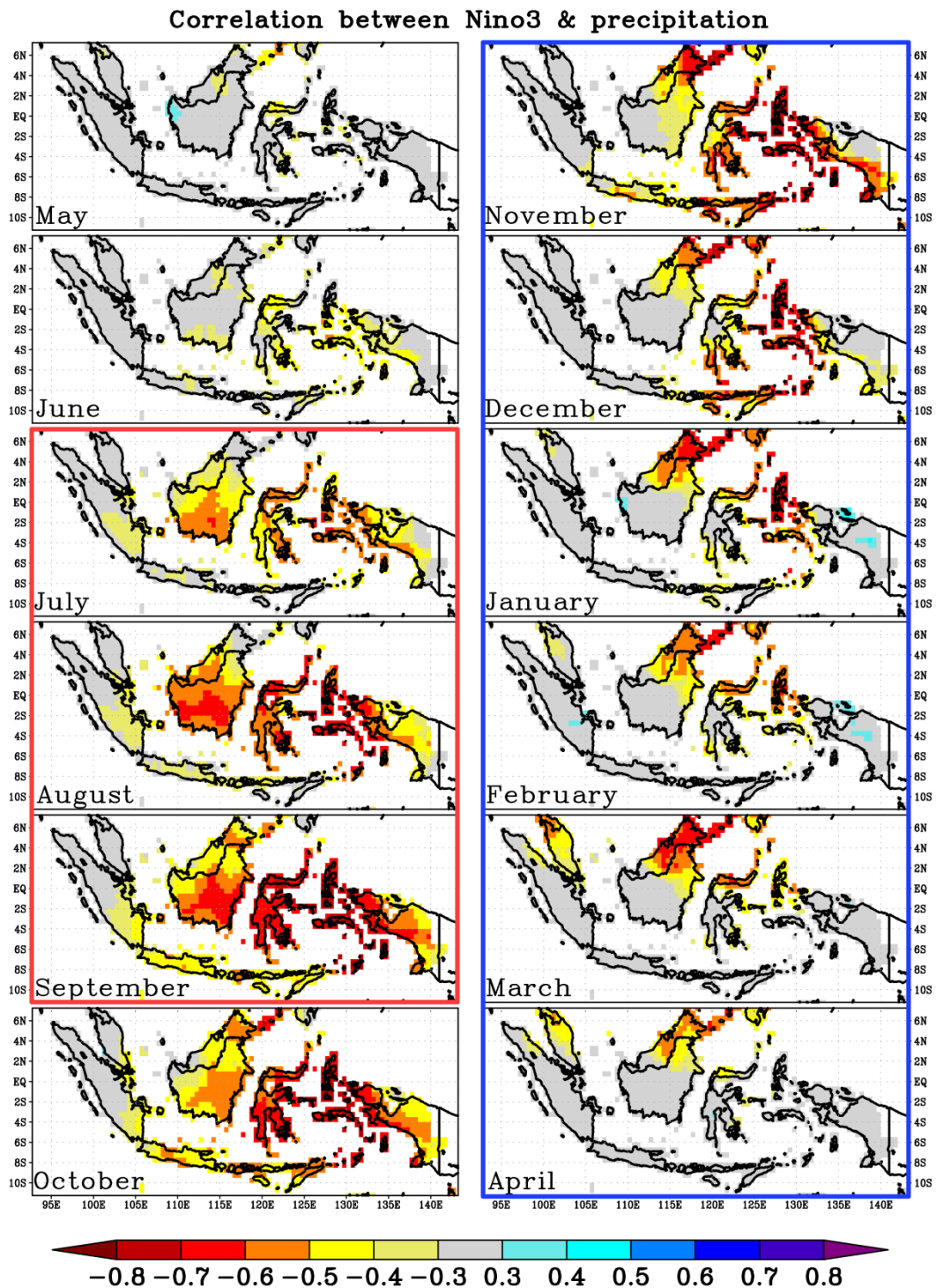
Figure 2.5. Spatial distribution of correlation coefficients of seasonal development of precipitation with normalized Niño-3. Correlations are calculated for 3-month averaged data, and the center month is written in each panel. Only correlations that are significant at the 95% confidence level are shown by the color shading. Red and blue frames indicate the dry and wet seasons, respectively.

Partial correlation between Nino3 & precipitation
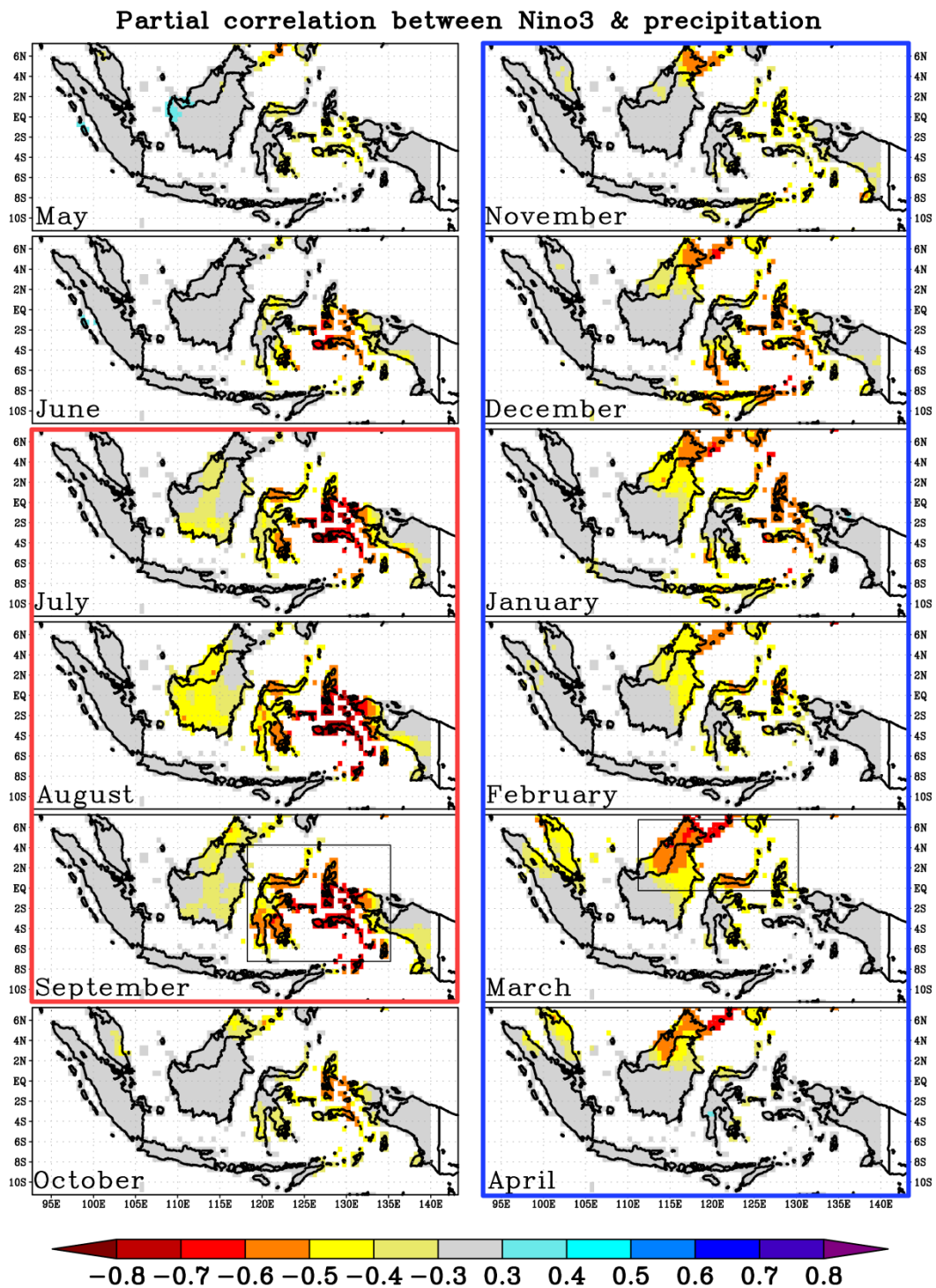
Figure 2.6. As in Fig. 2.5, but for partial correlation coefficients. The rectangular areas in September and March denote the regions for which the area-averaged precipitation is shown in Fig. 2.7.

Normalized time series

Sign—reversed area—averaged precipitation

Nino3

(a) Eastern Indonesia, September
$r = 0.71$

(b) Northern Indonesia, March
$r = 0.66$

Year
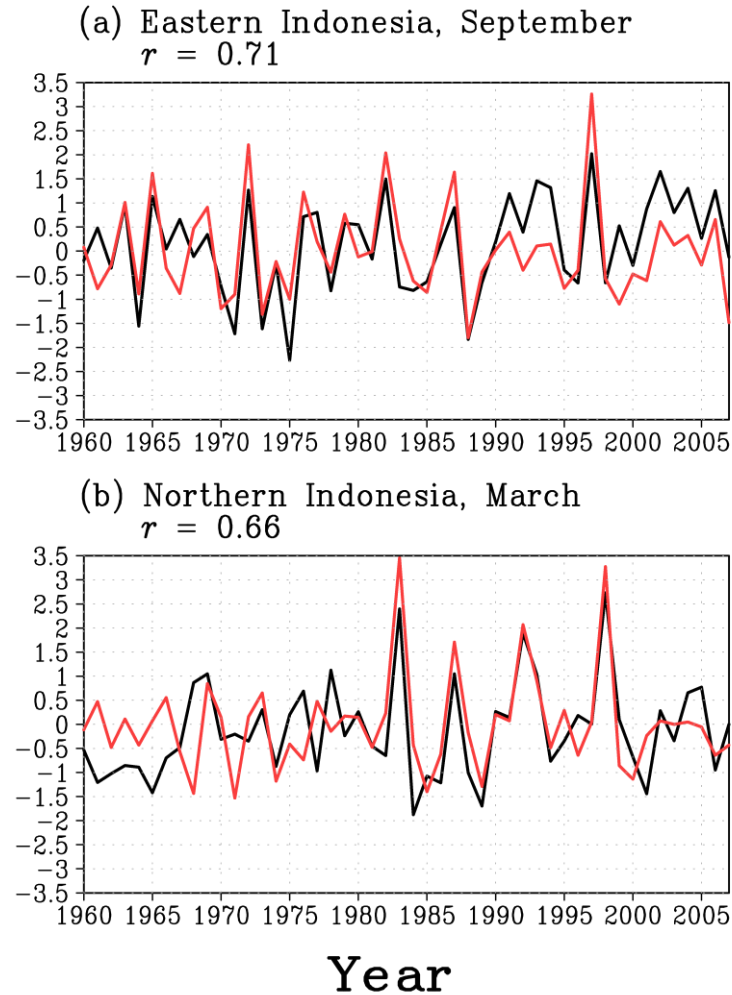
Figure 2.7. Time series of normalized Niño-3 and normalized and sign-reversed precipitation averaged over the area in Fig. 2.6, namely, (a) the rectangular areas in eastern Indonesia (118°–135°E, 7°S–4°N) between August and October and (b) northern Indonesia (111°–130°E, 0°–7°N) between February and April. The center month of the 3-month average is shown in the panel title for a consistency with other figures. The sign of precipitation is reversed for an easier comparison with Niño-3.

Partial correlation between Nino3
& moisture flux convergence

(a) September

(b) March
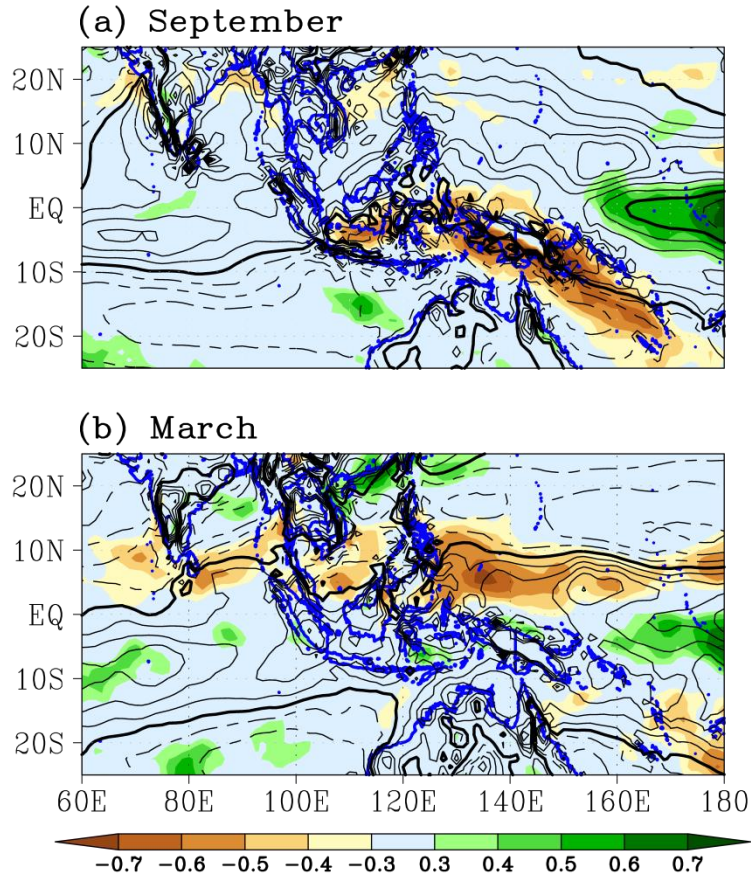
Figure 2.8. Spatial distribution of partial correlation coefficients between the vertically integrated moisture flux convergence and Niño-3 (shading) and climatology of the vertically integrated moisture flux convergence (contours; 10^{-4} kg m^{-2} s^{-1}) in (a) September and (b) March. Correlations and climatologies are calculated for 3-month averaged data, and the center month is shown in the panel title for consistency with other figures. Only correlations that are significant at the 95% confidence level are shown by the color shading. The solid (dashed) contours shown are 0.2, 0.4, 0.6, 0.8, and 1 (–0.2, –0.4, –0.6, –0.8, and –1), and the thick contour is the zero contour.
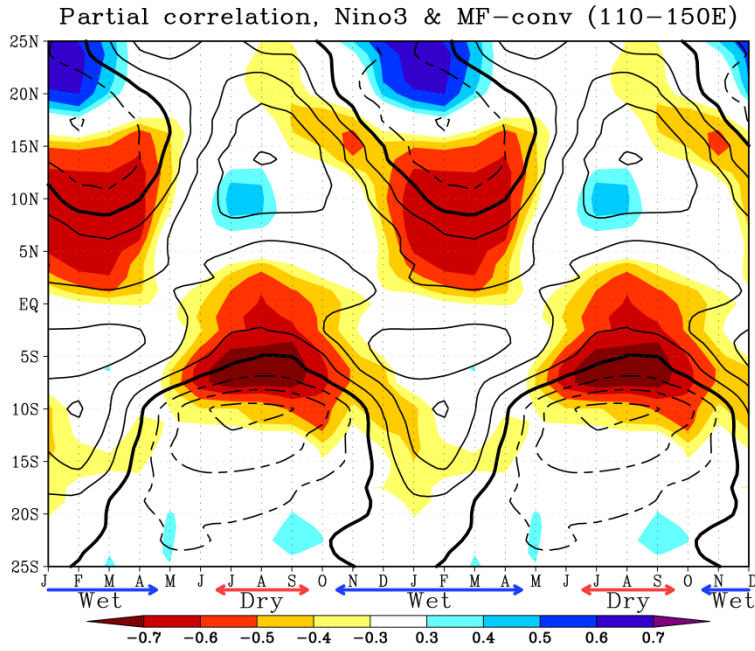
Figure 2.9. Time–latitude sections (110°–150°E) of partial correlation coefficients between the vertically integrated moisture flux convergence (MF-conv) and Niño-3 (shading) and climatological MF-conv (contours; 10^{-4} kg m^{-2} s^{-1}) for 3-month averaged data. Only correlations that are significant at the 95% confidence level are shown by the color shading. The solid (dashed) contours shown are 0.2, 0.4, 0.6, 0.8, and 1 (–0.2, –0.4, –0.6, –0.8, and –1), and the thick contour is the zero contour. Red and blue arrows indicate the periods of the dry and wet seasons, respectively. The x axis indicates the center month of the 3-month average.
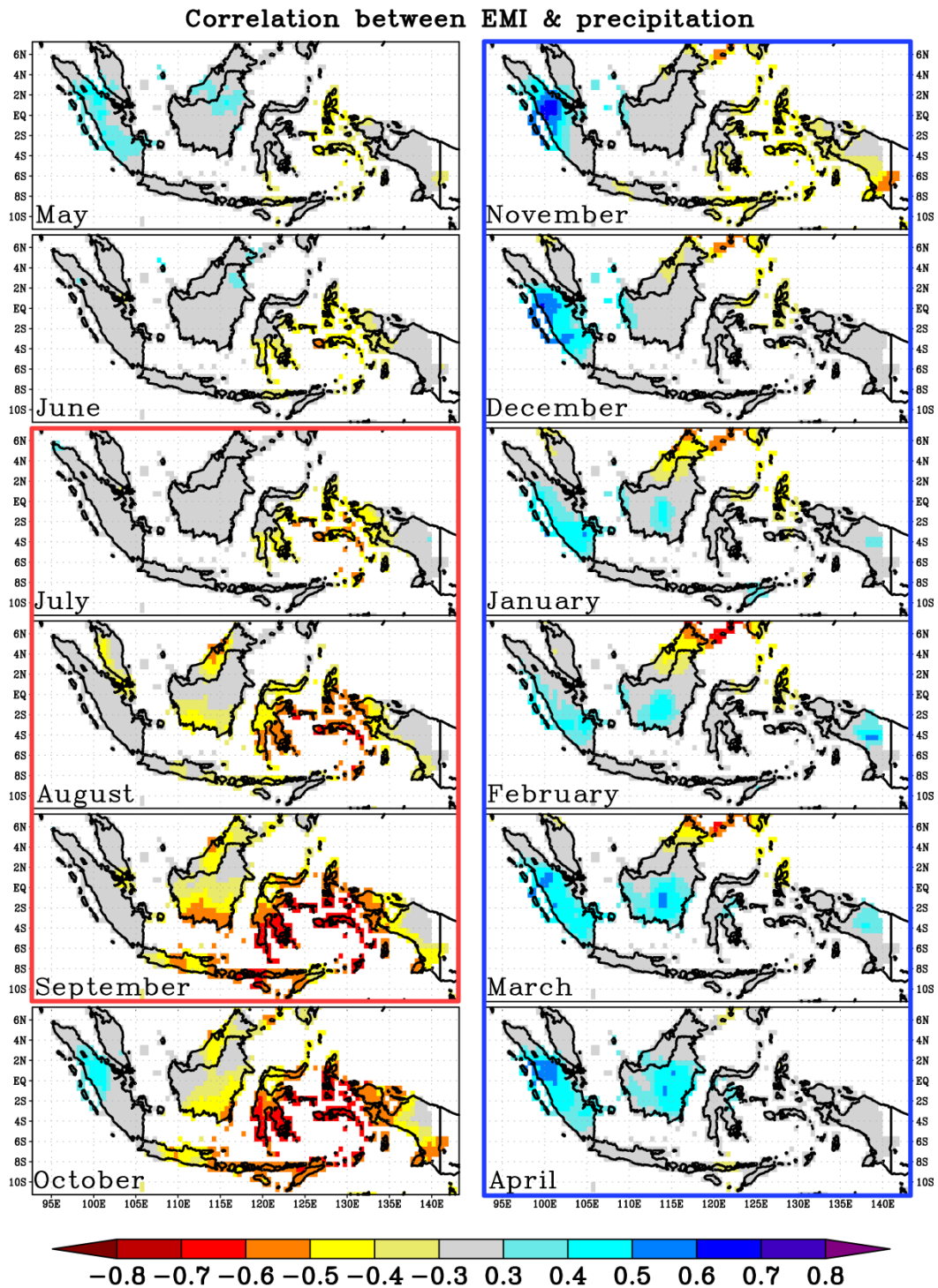
Figure 2.10. Spatial distribution of correlation coefficients of the seasonal development of the precipitation with normalized EMI. Correlations are calculated for 3-month averaged data, and the center month is written in each panel. Only correlations that are significant at the 95% confidence level are shown by the color shading. Red and blue frames indicate the dry and wet seasons, respectively.
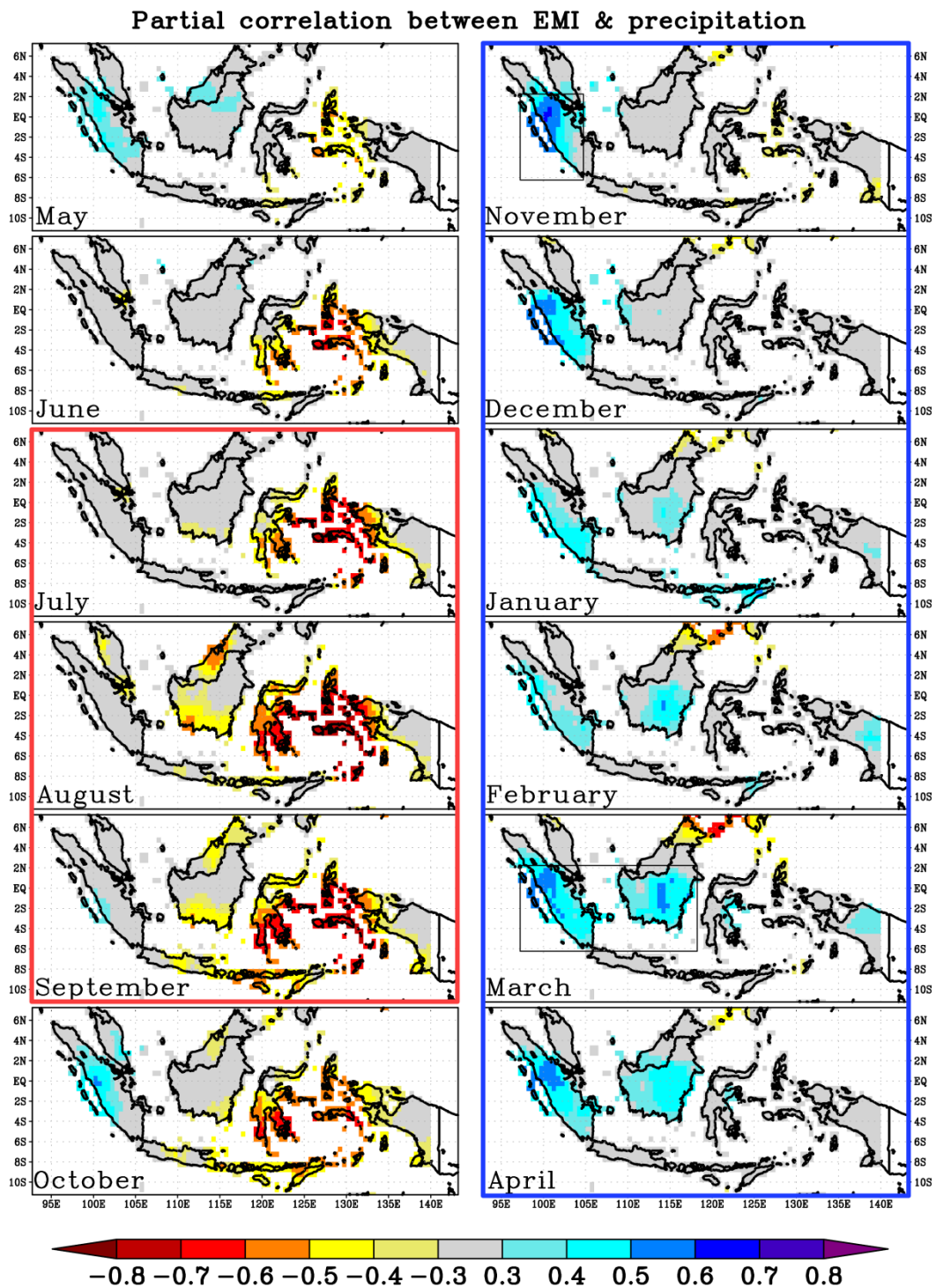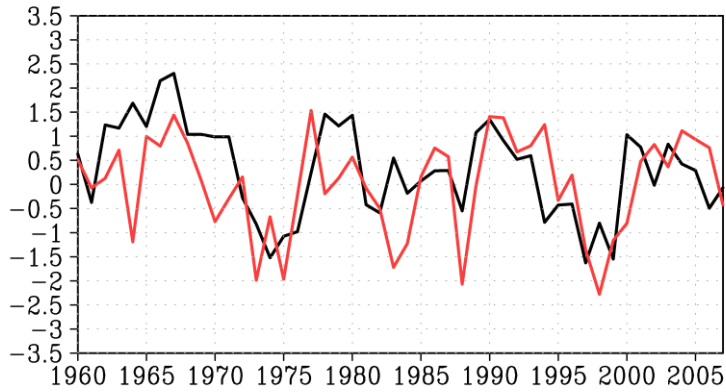
Figure 2.11. As in Fig. 2.10, but for partial correlation coefficients. The rectangular areas in November and March denote the regions for which the area-averaged precipitation is shown in Fig. 2.12.
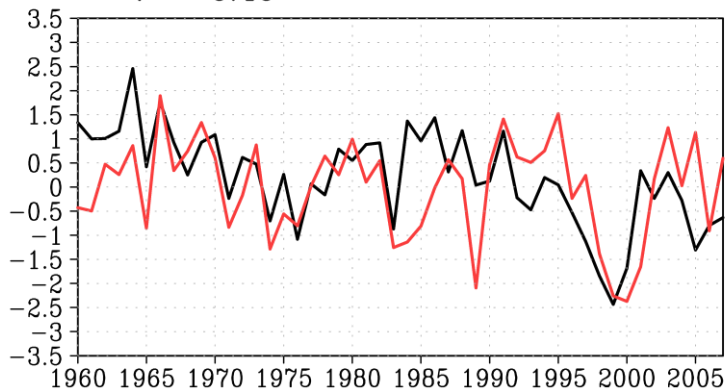
Normalized time series

─── **Area-averaged precipitation**

─── **EMI**

(a) Western Indonesia, November
$r = 0.47$

(b) Central-western Indonesia, March
$r = 0.46$

Year

Figure 2.12. Time series of normalized EMI and normalized precipitation averaged over the area in Fig. 2.11, namely, (a) the rectangular areas in western Indonesia (97°–105°E, 6°S–2°N) between October and December and (b) central to western Indonesia (97°–118°E, 6°S–2°N) between February and April. The center month of the 3-month average is shown in the panel title for consistency with other figures.

Partial correlation between EMI
& moisture flux convergence
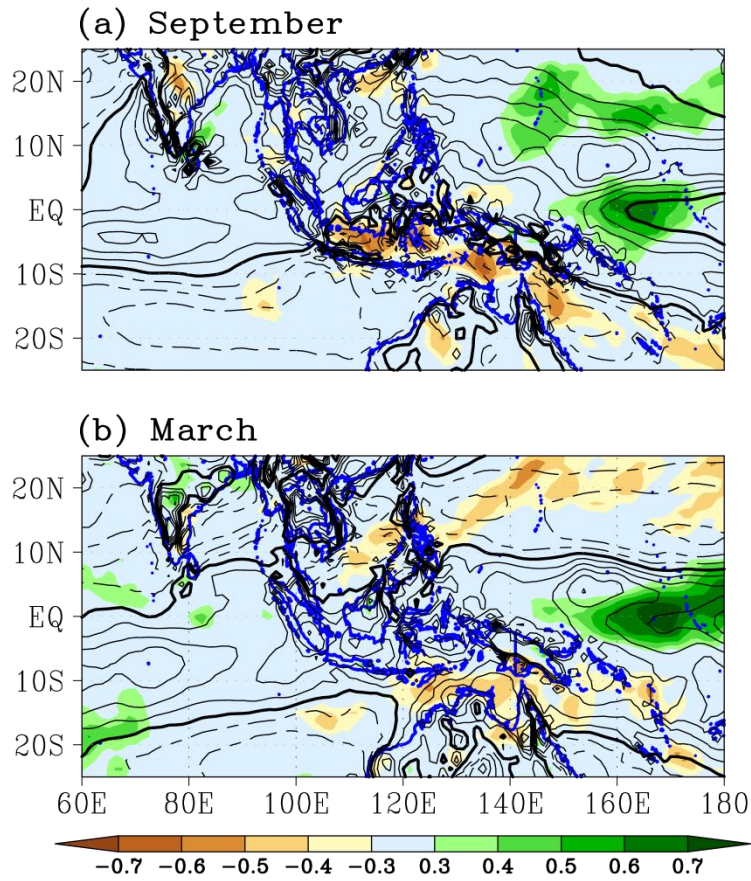
(a) September

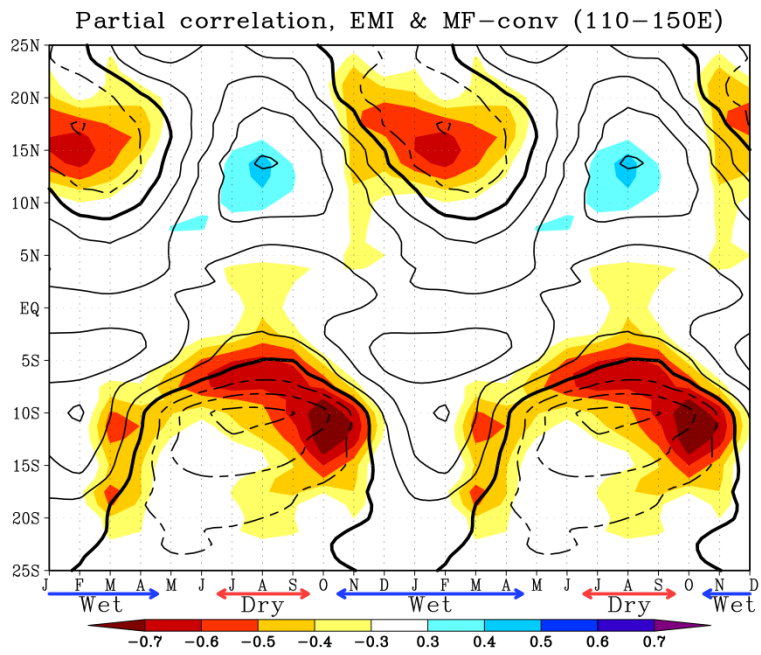(b) March

Figure 2.13. As in Fig. 2.8, but for EMI.

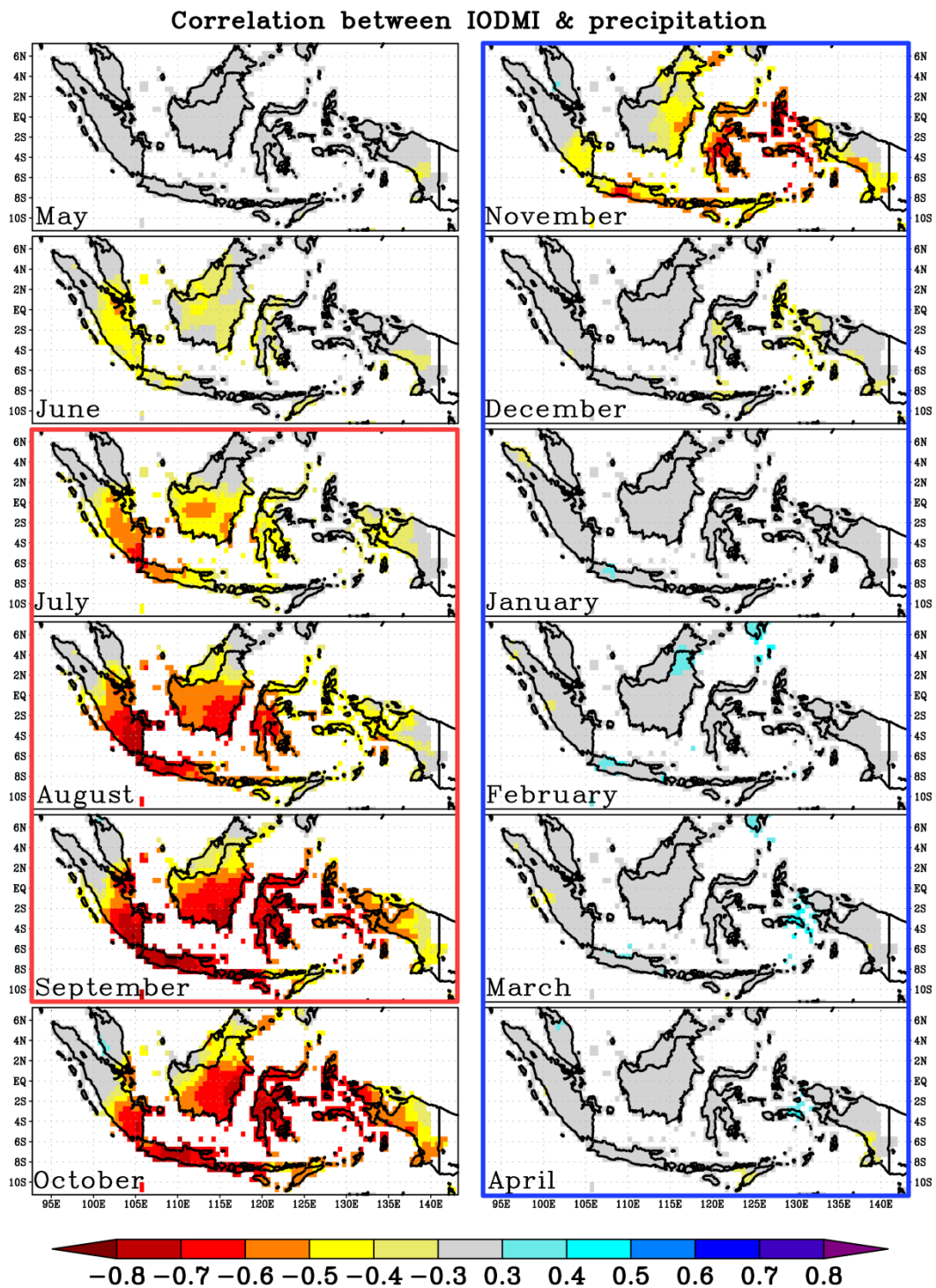Figure 2.14. As in Fig. 2.9, but for EMI.

Figure 2.15. Spatial distribution of correlation coefficients of the seasonal development of the precipitation with normalized IODMI. Correlations are calculated for 3-month averaged data, and the center month is written in each panel. Only correlations that are significant at the 95% confidence level are shown by the color shading. Red and blue frames indicate the dry and wet seasons, respectively.
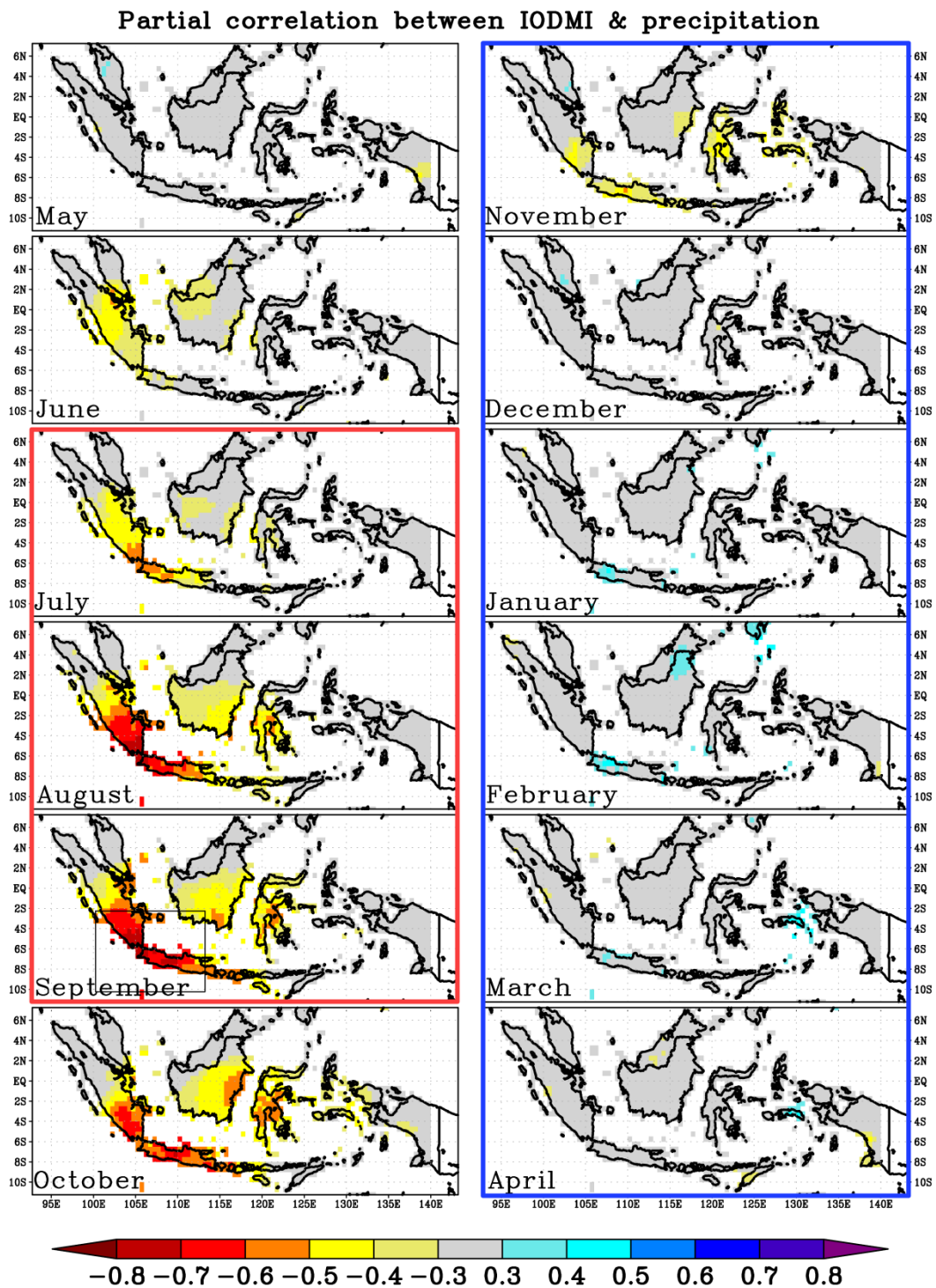
Fig. 2.16. As in Fig. 2.15, but for partial correlation coefficients. The rectangular area in September denotes the region for which the area-averaged precipitation is shown in Fig. 2.17.

Normalized time series
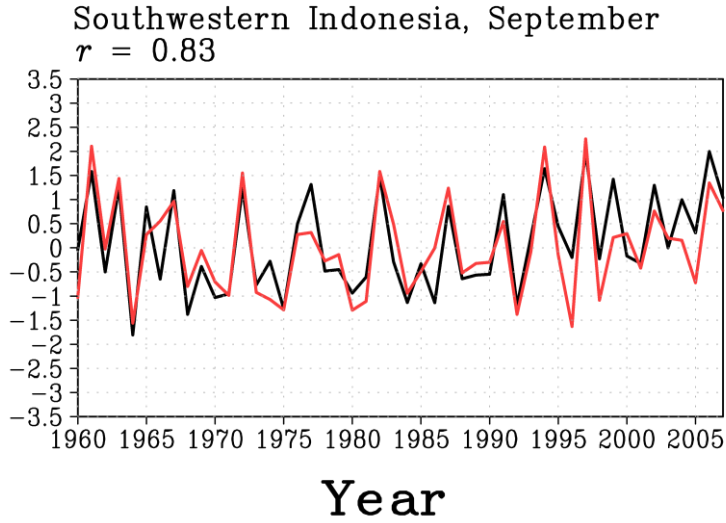
Figure 2.17. Time series of normalized IODMI and normalized and sign-reversed precipitation averaged over the area in Fig. 2.16, namely, the rectangular area in southwestern Indonesia (100°–113°E, 10°–2°S) between August and October. The center month of the 3-month average is shown in the panel title for consistency with other figures.

Partial correlation between IODMI
& moisture flux convergence
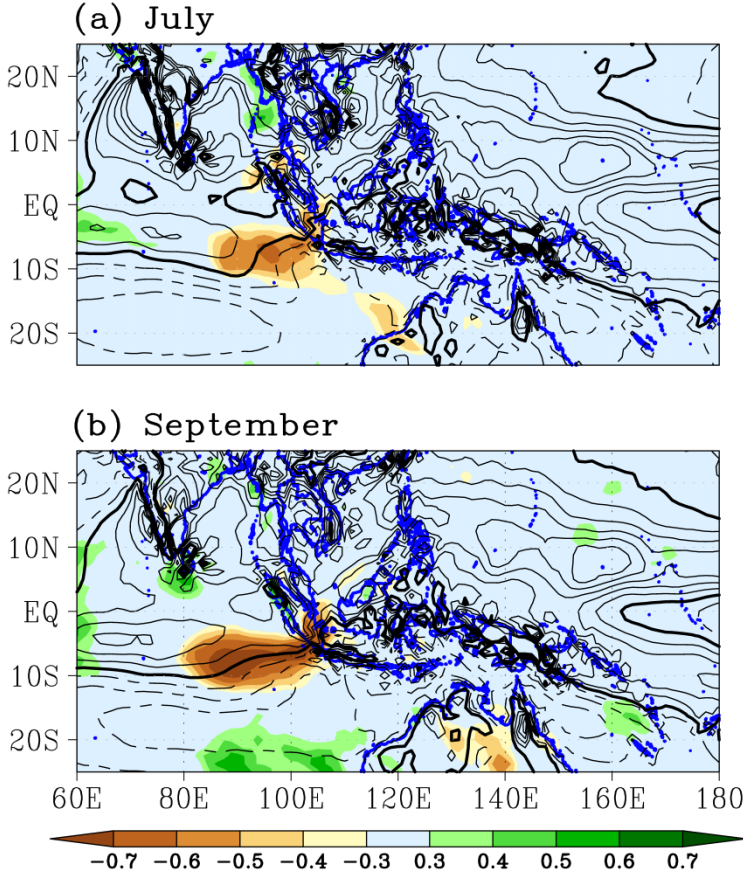
(a) July

(b) September

Figure 2.18. As in Fig. 2.8, but for IODMI in (a) July and (b) September.
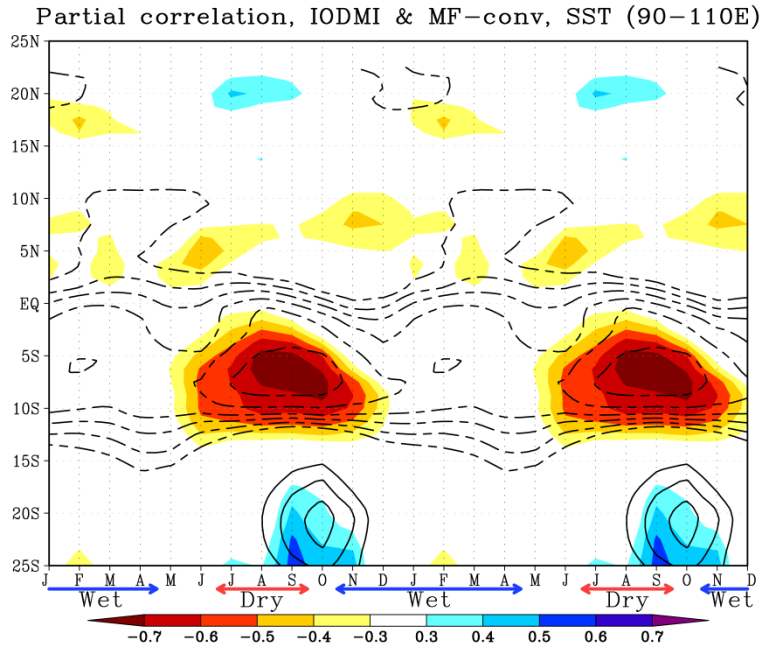
Fig. 2.19. Time–latitude sections (90°–110°E) of partial correlation between the vertically integrated moisture flux convergence (MF-conv) and IODMI (shading) and partial correlation between SST and IODMI (contours) for 3-month averaged data. Only correlations that are significant at the 95% confidence level are shown by the color shading. The solid (dashed) contours shown are 0.3, 0.4, 0.5, 0.6, 0.7, and 0.8 (–0.3, –0.4, –0.5, –0.6, –0.7, and –0.8). Red and blue arrows indicate the periods of the dry and wet seasons, respectively. The x axis indicates the center month of the 3-month average.

Chapter 3

Role of remote and local SSTA forcing in shaping interannual variations of precipitation over the Maritime Continent during El Niño

3.1. Introduction

The Maritime Continent (MC), which is made up of thousands of islands of various sizes and mountainous terrains (Fig. 3.1), sits in the pathway of the major monsoon systems (Qian et al. 2002; Hung et al. 2004) as well as gets affected by the large-scale climate mode in the tropics. This region can play a critical role in global climate variations (Ramage 1968; Neale and Slingo 2003). Climatologically, total precipitation over the MC region in boreal summer-autumn (say, from July to October; JASO) is mainly distributed to the north due to the active convergence zones in the region north of the equator. In contrast, from the boreal winter to spring (say, from January to April; JFMA), high precipitation is mainly concentrated over the southern hemisphere (SH) side of MC because of the seasonal migration of the active convergence zones to the south (Qian 2008). The El Niño-Southern Oscillation (ENSO), characterized by an abnormal sea surface temperature (SST) warming over the central-eastern tropical Pacific Ocean (Fig. 3.2), is a major factor in influencing the interannual variability of the MC's climate (Webster et al. 1998). A number of studies have investigated the relationship between El Niño and precipitation over this region (e.g., Haylock and McBride 2001; Hendon 2003; Chang et al. 2004; Giannini et al. 2007; Jia et al. 2016; Jian and Li 2018; Alsepan and Minobe 2020). El Niño tends to significantly reduce precipitation over the MC and causes some problematic socio-economic issues, such as crop failures and forest fires (Page et al. 2002; Waple and Lawrimore 2003; Pan et al. 2018).

El Niño influence exhibits some interesting seasonal dependencies and regional characteristics. It has been suggested that El Niño causes negative precipitation anomalies over the SH side of MC during the boreal summer-autumn and over the northern hemisphere (NH) side of MC during the boreal-winter-spring, and the seasonality of these precipitation features is largely controlled by the seasonal migration of the mean convergence zones (Alsepan and Minobe 2020). The right panels of Fig. 3.3 illustrate the observed anomalous precipitation pattern (defined as monthly deviations from an annual climatological cycle) over the MC region due to El Niño, which are obtained through regressions of precipitation anomalies against Niño-3.4 index (area-averaged SST anomaly over 120°–170°W, 5°S–5°N), during JASO and JFMA seasons along with the climatological vertically integrated moisture flux convergence between 1000-200 hPa. The mean convergence zone is located in the NH during the JASO season and in the SH during the JFMA season corresponding to its seasonal migration. Significant negative precipitation anomalies over the SH side of MC during the JASO season are only confined around the southern edge of the convergence zone. In the JFMA season, negative precipitation anomalies in the NH occur only around the northern edge of the convergence zone. This means that the seasonal-dependent precipitation responses over the MC to El Niño are strongly associated with the seasonal migration of the climatological convergence zones; that is, the precipitation anomalies occur only around the southern (northern) edge of the convergence zones in the JASO (JFMA) season and when one of the edges reaches the equator around 10°S–10°N range, consistent with Alsepan and Minobe (2020).

Given the distinctive life cycles of the anomalous precipitation, a key question to be answered is what is the relative contribution of remote and local SST anomaly (SSTA)

forcing in contributing to the observed seasonally-dependent precipitation anomaly patterns. During the active phase of El Niño, strong SST warming occurs in the tropical central-eastern Pacific (CEP), accompanied by significant SST cooling around the tropical western Pacific (WP) although its magnitude is much weaker than that in the tropical CEP (Fig. 3.2). However, since the mean SST in the tropical WP is much higher than in the tropical CEP, the atmosphere is expected to be more sensitive to the SST variations in the warm pool region than that in the equatorial cold tongue (Palmer and Owen 1986; Ju and Slingo 1995). It has been suggested that precipitation anomalies over the MC region during El Niño events may be associated with the changes of local SST since they are highly correlated (Hendon 2003; Wang et al. 2003; Lau and Nath 2003; Zhang et al. 2016; Xu et al. 2019). Thus, to clarify this issue, a model simulation study should be worthy of being conducted.

Some numerical simulation studies have been recently conducted by using the atmospheric general circulation model (AGCM). Stuecker et al. (2015) and Xie and Zhou (2017) studied the atmospheric responses over the tropical WP to El Niño by prescribing positive El Niño-related SSTA in the tropical CEP region with a constant amplitude (Niño-3.4 SSTA = 1.32°C) and climatological SST elsewhere in their AGCM. It was found that the boreal winter atmospheric circulations and the associated precipitation responses over the tropical WP are mainly generated by the remote SSTA forcing. However, local SSTA forcing in the tropical WP was not considered, and hence it is unclear whether the local forcing is essential. By separating the prescribed SSTA in the tropical CEP and WP, Wang et al. (2000) and Wu et al. (2010) found that both local and remote forcing are important in causing atmospheric anomalies and the associated precipitation anomalies over the tropical WP. Still, the prescribed local SSTA forcing is only limited for the NH side of MC

in their study without considering the local forcing over the southern areas (Fig. 3.2). Furthermore, these AGCM studies only focused on the boreal winter El Niño. As mentioned above, the precipitation responses over the MC to El Niño can vary seasonally.

Therefore, the objective of this study is to investigate the relative role of the remote versus local SSTA forcing in shaping seasonal-dependent precipitation responses over the MC region to El Niño during the JASO and JFMA seasons. Our strategy is to examine the response of an AGCM to regional SSTA forcing. As demonstrated in the next section, the AGCM used in this study is capable of reproducing the large-scale precipitation anomalies over the MC region during the El Niño events.

3.2. The model and a control simulation

We use the AGCM for the Earth Simulator (AFES) version 3 (Ohfuchi et al. 2004; Enomoto et al. 2008; Kuwano-Yoshida et al. 2010), which was developed by the Earth Simulator Center and Application Laboratory of the Japan Agency for Marine-Earth Science and Technology (JAMSTEC). AFES model is based on an AGCM developed jointly by the Centre for Climate System Research (CCSR) of the University of Tokyo and the Japanese National Institute for Environmental Studies (NIES) (Numaguti et al. 1997). Enomoto et al. (2008) improved the accuracy and efficiency of the Legendre transform and physical performance by introducing a new radiation scheme (MstrnX; Sekiguchi and Nakajima 2008) and cumulus convection scheme (Emanuel 1991; Emanuel and Živković-Rothman 1999; Peng et al. 2004). The model, as used in this study, introduced an improved probability density function (PDF) cloud scheme (Kuwano-Yoshida et al. 2010). This version of the model has a dynamical core of the hydrostatic spectrum model with σ coordinate. The subgrid-scale exchange of heat, momentum, and moisture is accomplished

using a turbulent closure scheme (MYNN level-2; Nakanishi and Niino 2004), and the land surface process is represented by the Minimal Advanced Treatments of Surface Interaction and Runoff (MATSIRO) model (Takata et al. 2003).

The AFES model has been extensively used in some studies. Most of those studies used the model for mid- and high-latitude air-sea interactions (Minobe et al. 2008; Ogawa et al. 2012; Kuwano-Yoshida and Minobe 2017; Okajima et al. 2018), ensemble-based data assimilation (Miyoshi and Yamane 2007; Miyoshi et al. 2007), and weather predictability (Kuwano-Yoshida and Enomoto 2013; Sato et al. 2017). Within the tropics, the AFES model was used for the study of tropical cyclones (Yoshioka et al. 2005; Oouchi et al. 2006; Yoshioka and Kurihara 2008) and their interannual variability related to canonical and Modoki El Niños (Ogata et al. 2021).

In the present study a spectral T239 resolution, which is approximately 50-km interval, with 32 sigma levels vertically from the surface to approximately 10 hPa is employed. For a control (CNTL) run, the model is integrated for 30 years from 1 March 1982 to 29 February 2012, and the initial atmospheric condition for the horizontal velocity, geopotential height, temperature, and specific humidity is taken from the Japanese 55-Year Reanalysis (JRA-55) dataset (Kobayashi et al. 2015). In the bottom boundary conditions, observed SST fields from the 0.25° daily Optimum Interpolation Sea Surface Temperature version 2 (OISST; Reynolds et al. 2007) are imposed over the global ocean. The monthly climatological ozone and aerosol are based on atmospheric model intercomparison project 2 (Liang et al. 1997) and spectral radiation-transport model for aerosol species (SPRINTARS; Takemura et al. 2005), respectively. The carbon dioxide concentration is at a constant mixing ratio of 348 ppmv, and the insolation is given as a constant of 1365 W m^{-2}.

The model is generally capable of simulating the substantial features of seasonal-dependent precipitation responses to El Niño. The left panels of Fig. 3.3 show the precipitation anomalies in the CNTL run through regressions against the Niño-3.4 index during the JASO and JFMA seasons. Compared with the observed features (the right panels of Fig. 3.3), the model can capture the large-scale precipitation anomaly patterns over the MC region and its seasonal dependency reasonably well, although it has systematic errors in some areas. For instance, it captures distinct precipitation responses in different regions and seasons. Similar to the observed, the simulated negative precipitation anomalies occur mainly over the SH side of MC during the JASO season and over the NH side of MC during the JFMA season, and these anomalies are only confined around the southern edge and northern edge of the convergence zones, respectively.

It is important to ascertain that one ensemble simulation, which is an arbitrary choice of 14 equivalent ensembles in the AFES model as CNTL, is reasonable enough to be used in this study. Figure 3.4 shows the comparison of the area-averaged precipitation time series between 14-ensemble mean, 1-ensemble as used in the CNTL run, and 13-ensemble member with slightly different in the initial atmospheric states for the SH (NH) side of MC during the JASO (JFMA) season. The CNTL run and other ensemble members show common interannual variability around the ensemble mean in both seasons. Precipitation anomalies due to El Niño are well simulated in all members, including large precipitation reductions during 1982/1983 and 1997/98 extreme El Niños. The correlation coefficient between the time series in the CNTL run and ensemble mean reaches more than 0.9 for both seasons. Therefore, these results suggest that one ensemble for the AFES model is reliable to represent the interannual variations of precipitation over the MC region associated with the El Niño events.

3.3. Experiment configuration

Given that the AFES model is capable of reproducing realistic El Niño influences on precipitation anomalies over the MC, we investigate the relative role of the remote and local SSTA forcing in generating these precipitation anomalies. We specially design the following two experiments to isolate the role of the SSTA forcing over the tropical central-eastern Pacific (CEP) and tropical western Pacific (WP). These experimental designs generally follow Su et al. (2001) and Li et al. (2005), who studied the tropical teleconnection and local response to SSTA during the 1997/98 El Niño.

In the first experiment (NoTroCEP), the climatological SST field is specified in the tropical CEP region (160°E–70°W, 30°S–40°N; see the box in Fig. 3.2a) while the observed SST is specified elsewhere. The purpose of this experiment is to examine the possible impacts of local SSTA on the atmosphere in the tropical WP region during El Niño. In the second experiment (NoTroWP), climatological SST is specified in the tropical WP region (90°–160°E, 30°S–40°N; see the box in Fig. 3.2b) while the observed SST is specified elsewhere. This experiment is expected to reveal the possible direct influences of remote SSTA forcing in the tropical CEP region. For each experiment above, the model is integrated for 30 years from 1 March 1982 to 29 February 2012 with the same initial conditions as in the CNTL run. The time interval of the model output is 6-hour.

A more conventional way of designing these experiments would have been to describe an experimental integration with observed SST over the regions of interest and climatological SST over the other areas. For example, observed SST is specified over the tropical CEP (WP) region, while climatological SST is specified elsewhere to isolate the sole influences of remote (local) SSTA forcing. The results would be the same as in the aforementioned experiment configuration if the system is linear, but they can be different

if it is nonlinear. However, when we examined an extreme El Niño in 1982/83 using conventional settings, we found a very large nonlinear effect in some regions, especially during the JASO season (figure not shown). Thus, we are convinced that the designs used in this study can be safer than the conventional ones.

3.4. Relative role of remote versus local SSTA forcing

3.4.1. JASO season

First, we present simulation results for the JASO season. Figure 3.5 shows precipitation anomalies and the associated SST and low-level wind anomalies due to El Niño, which are obtained through regressions against the Niño-3.4 index. In the CNTL run (Fig. 3.5a), negative precipitation anomalies are induced over the SH side of MC around the southern edge of the convergence zone. These precipitation anomalies are related to the occurrence of low-level anomalous equatorial westerly wind and off-equatorial twin-cyclone over the tropical WP (Fig. 3.5b), a reminiscent of the Matsuno-Gill pattern due to anomalous positive heating (Matsuno 1966; Gill 1980). By removing such remote forcing, the corresponding precipitation anomalies as well as low-level atmospheric circulation anomalies in the NoTroCEP experiment (Figs. 3.5c-d) are largely suppressed compared to that in the CNTL run, although local negative SSTA is still present in NoTroCEP. In contrast, if only local SSTA forcing is removed in NoTroWP (Figs. 3.5e-f), similar precipitation and wind circulation anomalies are well reproduced as in CNTL. This result indicates that the sole effect of remote SST warming in the tropical CEP is critical in causing anomalous negative precipitation over the SH side of MC during the JASO season and local SST cooling plays no significant roles.

To know better the relation between precipitation and El Niño for the precipitation anomalies over the SH side of MC due to El Niño, we plot the normalized time series of area-averaged precipitation anomalies and Niño-3.4 index for the JASO season (Fig. 3.6). Close covariability is apparent between the precipitation time series for both CNTL and NoTroWP and Niño-3.4 index (Figs. 3.6a,c), whereas the correlation becomes very weak and insignificant for NoTroCEP (Fig. 3.6b). The comparison between the time series of all experiments with the Niño-3.4 index again highlights the essential tropical CEP SSTA contributions to the interannual variations of precipitation over the SH side of MC during this season. For example, during 1997, known as a super El Niño (McPhaden 1999), large precipitation reduction with more than two standard deviations only occurs if the remote SSTA forcing is prescribed in the model, regardless of whether the local SSTA is included or not (Figs. 3.6a,c).

In order to illustrate how El Niño directly induces negative precipitation anomalies over the SH side of MC during the JASO season under the viewpoint of water budget, Figure 3.7 shows JASO-mean 925 hPa climatological specific humidity and anomalous horizontal wind regressed onto Niño-3.4 index. Please note that for this season and the JFMA season (see section 3.4.2) we ignore the local evaporation changes and thermodynamic processes for the mechanisms of precipitation anomalies because they are small (figure not shown). The level of 925 hPa is chosen because most moisture is confined in the planetary boundary layer. The spatial pattern of climatological specific humidity generally resembles the climatological boreal summer-autumn convergence zone (Fig. 3.3), where warm and moist air is located in the NH accompanied by cold and dry air to the south. Note that the climatological specific humidity has a strong meridional gradient over the SH. The anomalous southwesterly wind component to the western flank of the

southern branch of cyclonic anomaly (Figs. 3.7a,c), which is directly induced by remote SSTA forcing, then advects the dry air into the SH side of MC, which in turn decreases precipitation there (Figs. 3.5a,e).

The seasonal dependence of the El Niño connectivity across the western and eastern tropical Pacific can be discerned from the ascending or descending branches of the anomalous Walker circulation between the eastern and western equatorial Pacific. Figure 3.8 shows anomalous vertical pressure velocity regressed onto the Niño-3.4 index averaged at 15°S–5°N during the JASO season. One of the salient features of the anomalous Walker circulation during El Niño is the ascending branch in the tropical CEP region (Figs. 3.8a), which can be attributed to the forcing of positive SSTA. Another essential feature is the anomalous downward motion over the MC region, associated with a suppressed convection there. In the absence of remote positive SSTA forcing, these anomalous Walker Circulation patterns disappear entirely (Fig. 3.8b). It is then suggested that by comparing NoTroCEP and NoTroWP experiments (Figs. 3.8b,c) the occurrence of anomalous downward motion over the tropical WP is forced directly by the remote SSTA as a compensation for the anomalous upward motion in the tropical CEP region.

Therefore, the numerical experiments above reveal the primary factor in causing precipitation reductions over the SH side of MC due to El Niño during the JASO season; that is, the tropical CEP SSTA exerts its remote influences on the MC's climate. In response to strong positive SSTA over the tropical CEP, twin Rossby wave cyclonic anomalies are induced in the off-equatorial WP. The southern branch of the twin-cyclonic anomaly advects dry air into the SH side of MC and then suppresses convection and precipitation. To the author's knowledge, this is the first AGCM study to reveal the sole effect of remote El Niño-related SSTA on MC's precipitation in the boreal

summer-autumn season, whereas the underlying local SSTA has no significant contributions.

3.4.2. JFMA season

In this section, we present the simulation results for the JFMA season. Figure 3.9 shows anomalous precipitation and the associated SST and low-level wind circulation regressed onto the Niño-3.4 index. CNTL simulation in Fig. 3.9a captures the negative precipitation anomalies around the northern edge of the convergence zone over the Philippines and around as in observed features (Fig. 3.3d). The Matsuno-Gill pattern, namely, off-equatorial twin-cyclonic anomalies and associated equatorial westerly anomalies, in this season (Fig. 3.9b) withdraws eastward compared to that in the JASO season (Fig. 3.5b), and this feature is caused by the temporal evolution of the mean convergence zone in the Pacific sector (Wu et al. 2017b). Another important atmospheric condition during this season is the occurrence of anticyclonic anomalies around the Philippine Sea (Fig. 3.9b). This anomalous anticyclone occurs roughly at the same position as the suppressed precipitation, suggesting that it is local response to the negative heating anomalies in the eastern Philippine Sea. If we remove the remote SSTA forcing over the tropical CEP, the anomalous negative precipitation and the associated anticyclone bear close similarity as in the CNTL run (Figs. 3.9a-d), whereas the Matsuno-Gill response in the tropical CEP disappears. The magnitude of area-averaged precipitation anomalies over the NH side of MC (red boxes in Fig. 3.9) for NoTroCEP reaches about 75% of that in the CNTL. In contrast, by removing the in-situ SSTA over the tropical WP, the Matsuno-Gill response remains, but the negative precipitation anomalies around the Philippines are significantly reduced, i.e., the area-averaged precipitation anomalies only reaching about 25% of that in the CNTL, associated with the

weakened anticyclonic anomalies (Figs. 3.9e-f). These results imply that local SST cooling over the tropical WP is a dominant factor in inducing negative precipitation anomalies over the NH side of MC during the JFMA season, and remote SSTA forcing may have a relatively small contribution.

The normalized anomalous precipitation time series averaged over the NH side of MC for all simulations is compared with the normalized Niño-3.4 index for the JFMA season (Fig. 3.10). Precipitation time series in CNTL and NoTroCEP experiments is highly correlated with the El Niño index (Figs. 3.10a-b), although the remote SSTA forcing is absent in NoTroCEP. This again emphasizes the important roles of local SSTA forcing in causing interannual precipitation variations over the NH side of MC due to El Niño. On the other hand, in NoTroWP (Fig. 3.10c) the correlation between precipitation time series and the Niño-3.4 index is still significant but much weaker compared to those in the other simulations because of the absence of in-situ SSTA forcing.

How the local SSTA forcing during El Niño induces negative precipitation anomalies over the NH side of MC for the JFMA season is described below. Figure 3.11 shows climatological specific humidity along with anomalous horizontal wind regressed against Niño-3.4 index at 925 hPa in the JFMA season. The warm and moist air is mainly located in the SH during this season associated with the southward migration of the convergence zones, leading to cold and dry air in the NH. The anomalous northeasterly wind in the NH then transfers the dry air into the NH side of MC, where the meridional gradient of climatological specific humidity is large (Fig. 3.11a), and reduces local precipitation (Fig. 3.9a). We may notice that the anomalous northeasterly wind is attributed to two low-level wind circulation anomalies; that is, the eastern flank of anticyclonic anomaly in the Philippine Sea and the western flank of cyclonic anomaly to

the east (Fig. 3.11a). However, the numerical experiments suggest that the anomalous advection by the eastern flank of anomalous anticyclone, which is mainly induced by local SSTA forcing (Fig. 3.11b), plays more important role than the western flank of anomalous cyclone (Fig. 3.11c) in causing precipitation anomalies over the NH side of MC (Figs. 3.9c and 3.9e, respectively).

Thus, the above results suggest that local SSTA forcing during El Niño in the JFMA season are necessary for causing anomalous negative precipitation over the NH side of MC. The negative precipitation anomaly is mainly induced by the dry air carried out by the eastern flank of the anticyclonic anomaly in the NH areas. These findings support those of Wang et al. (2000) and emphasize in more detail how the local SSTA can contribute to the precipitation anomalies in the tropical western North Pacific during the boreal winter-spring El Niño.

3.5. Summary and discussion

We have investigated the relative contribution of remote versus local SSTA forcing during El Niño in shaping the interannual variations of precipitation over the Maritime Continent (MC) region by conducting AGCM experiments using the AFES model. Although several studies have examined the connectivity between the western and eastern tropical Pacific and local response to SSTA forcing during El Niño events (see section 3.1), given that the precipitation response over the MC region has a distinct characteristic spatially and temporally, the present study provides a more comprehensive understanding of seasonal-dependent precipitation responses to the remote and local SSTA forcing during the boreal summer-autumn (JASO) and winter-spring (JFMA) season.

The precipitation responses to regional El Niño-related SSTA exhibit interesting differences between the two seasons. In the JASO season, anomalous negative precipitation mainly occurs over the southern hemisphere (SH) side of the MC region, which is only confined around the southern edge of the convergence zones (Figs. 3.3a,c). The numerical experiments reveal that these precipitation anomalies are likely explained as a direct or remote influence of El Niño. In response to strong SSTA over the tropical CEP, off-equatorial twin Rossby wave cyclonic anomalies are induced in the tropical WP (Figs. 3.5b,f). The anomalous southwesterly wind component to the western flank of the twin cyclonic anomalies advects dry air into the SH side of MC (Figs. 3.7a,c), which then suppresses the convection and precipitation there. During the JFMA season, the precipitation anomalies are only confined in the northern hemisphere (NH) side of MC around the northern edge of the convergence zones (Figs. 3.3b,d), and local SSTA forcing is important in causing these precipitation anomalies. In-situ SST cooling in the tropical WP favors the generation of anticyclonic anomalies over the Philippine Sea (Fig. 3.9d). The anomalous northeasterly wind component to the eastern flank of the anomalous anticyclone transfers dry air into the NH side of MC (Fig. 3.11b) and reduces local convection and precipitation.

Our numerical simulations generally confirm the findings reported by Wang et al. (2000) and Wu et al. (2010) for the role of regional SSTA forcing during El Niño to precipitation anomalies over the MC region in the JFMA season. Although the prescribed local SSTA forcing in their study is only limited to the NH side of MC rather than covering both NH and SH sides as we imposed in the model, the contribution of local forcing to precipitation anomalies is larger than the remote forcing as found in the present results. However, there are still important differences. For example, the amplitude of

area-averaged precipitation anomalies over the NH of MC induced by local SSTA forcing is about 75% of that in the CNTL run, but is limited to only 50% in Wang et al. (2000). Furthermore, our study provides more detail explanation on how the Philippine Sea anticyclonic anomalies, which is mainly induced by local ocean cooling, generate negative precipitation anomalies over the NH of MC during El Niño.

The AFES model generally reproduces the substantial features of seasonal-dependent precipitation responses over the MC to El Niño as in the observation (Fig. 3.3). However, a notable deficiency is found in the JFMA season. The model underestimates precipitation anomalies to the southeast of the Philippine Sea compared to the observed (Figs. 3.3b,d). This may be partly due to the excess mean precipitation in the model (Kodama et al. 2019). Good et al. (2020) suggested that a possible reason for such limitation is due to a lack of representation of shallow circulation in a numerical simulation. Improving the convective scheme in the AFES model by considering a closure for shallow convection might considerably improve the simulated mean precipitation and its interannual variability (Baba 2020). Nevertheless, the present results can explain how the local SSTA forcing contributes to the precipitation anomalies over the MC region through large-scale atmospheric dynamic processes.

Regression analysis method used in this study can become a limitation owing to the asymmetry between El Niño (warm event), and its counterpart, namely, La Niña (cold event). It has been suggested that El Niño and La Niña can have a significant asymmetry in amplitude, structure, and temporal evolution (Hoerling et al. 1997; Burgers and Stephenson 1999; Kang and Kug 2002; Jin et al. 2003; An and Jin 2004; Wu et al. 2010; Chen et al. 2015; Chen and Li 2021). The anomalous convection over the equatorial central-eastern Pacific during La Niña shifts westward compared to that during El Niño

(Hoerling et al. 1997), and thus may result in different precipitation responses over the MC region between El Niño and La Niña. Numerical simulation studies indicated that this asymmetry could be attributed to the nonlinear atmospheric responses to the underlying SSTA (Hoerling et al. 1997; Kang and Kug 2002). Therefore, further studies are necessary to investigate the asymmetric precipitation features over the MC between El Niño and La Niña events.

Although we have examined the influence of El Niño, other tropical climate modes in different basins might also contribute to the interannual variations of precipitation over the MC region. For example, the Indian Ocean Dipole (IOD) mode (Saji et al. 1999), which is often coinciding with the El Niño events, exerts its significant impacts on the MC during the boreal summer-autumn season (Alsepan and Minobe 2020). This influence can be seen in the NoTroCEP experiment in the JASO season (Fig. 3.5c). A small portion of significant precipitation reductions occurs in the eastern pole of the IOD even though the remote positive SSTA over the tropical CEP is removed. Nonetheless, we have shown that in this season remote El Niño-related positive SSTA is the primary factor in reducing large-scale precipitation over the SH side of the MC region regardless of whether the local SSTA forcing is available or not (Figs. 3.5c-f).

Another major climate mode in the tropical Indian Ocean is basinwide warming. It is generated mainly during the peak of El Niño in the boreal winter (Fig. 3.2b) and persists until the following summer when El Niño vanishes (Xie et al. 2009). To test the possible effects of this climate mode, we examine an extreme El Niño event in 1982/83 by prescribing the climatological SST over the tropical WP and CEP region and the observed SST elsewhere. This experiment is expected to reveal the influence of remote SSTA forcing over the tropical Indian Ocean on the precipitation anomalies over the NH side of

65

MC during the boreal winter. The result suggests that the Indian Ocean basin-wide warming only has small contributions to the precipitation anomalies during this single extreme El Niño event (figure not shown), consistent with previous studies for El Niño composites (Wang et al. 2000; Wu et al. 2012; Chen et al. 2016). At present, it is widely accepted that basinwide warming plays a crucial role in the MC's climate during the boreal summer following El Niño through the Indian Ocean capacitor effect (Xie et al. 2009; Xie et al. 2016; Xie and Zhou 2017).

The use of the coupled model for the present study is interesting to discuss, considering that in reality the ocean is coupled with the atmosphere over the tropical region (Wang et al. 2004). When we use a coupled model, however, SST is an internal variability and thus cannot be treated as the forcing. Therefore, the use of the coupled model is difficult for the present purpose (see section 3.1). Furthermore, Wu and Kirtman (2005, 2006) showed that SST-forced AGCM run is more accurate than freely coupled models for simulating tropical precipitation during El Niños. This is probably related to the inadequate simulations of El Niño SSTs in the coupled models (Bellenger et al. 2014). These results indicate that rather than the deficiency arising from the inaccurate SST forming mechanisms with the use of the AGCM, i.e., SST is not always the forcing of the atmosphere, but SST is also forced by the atmosphere, the erroneous simulation of the El Niño in the coupled models causes larger biases in tropical precipitations. Such a problem can be relaxed by a relatively new experiment design for the coupled model, called pacemaker experiment (Kosaka and Xie 2016), by nudging ocean surface temperature in a limited region (say, central-eastern Pacific) to the observed temperature (Wu et al. 2017a, 2017b; Wang et al. 2018). Still, using a pacemaker experiment will not be possible to examine the separated influences of the tropical western Pacific SSTs and the tropical central-eastern Pacific SSTs because these two regions are strongly related in the coupled model.
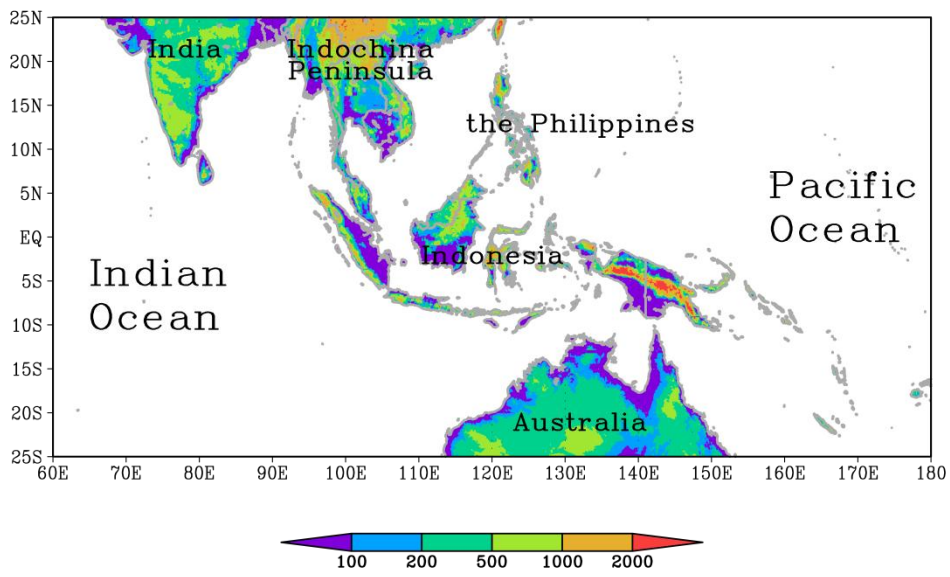
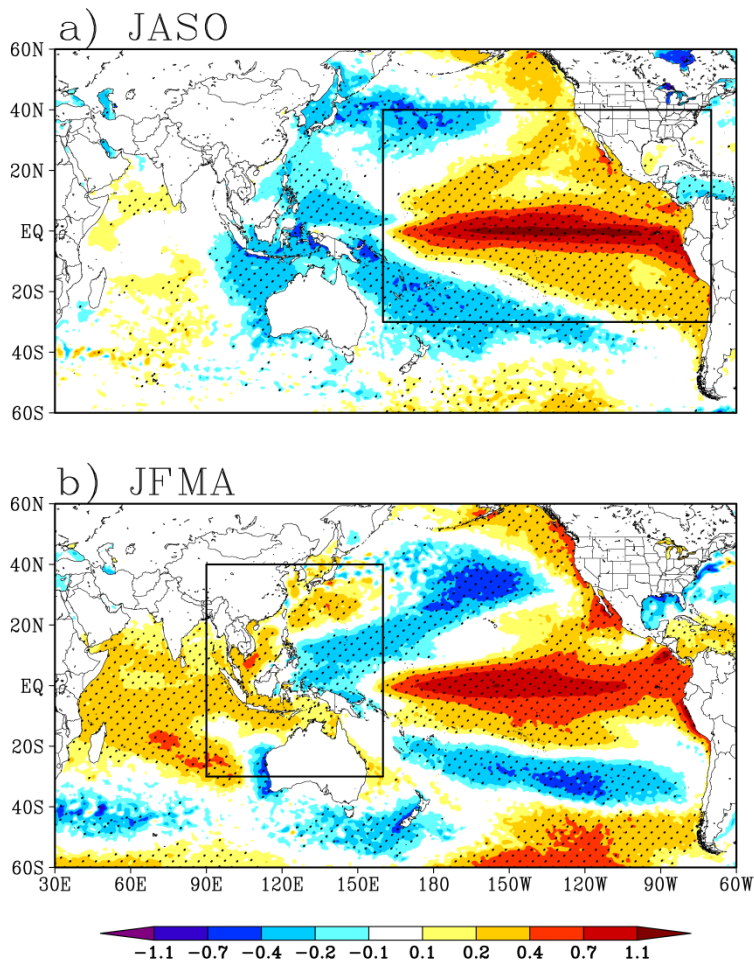Figure 3.1. Topographic map (m) of the study area based on the Worldbath dataset (http://ingrid.ldgo.columbia.edu/SOURCES/.WORLDBATH/.bath/).

Fig. 3.2. Spatial distribution of anomalous SST (°C) regressed against normalized Niño-3.4 index for (a) JASO and (b) JFMA season with use of the OISST data. Dots denote the values that are significant at the 95% confidence level. Geographic location in (a) and (b) represents the tropical central-eastern Pacific (CEP) and western Pacific (WP), respectively.
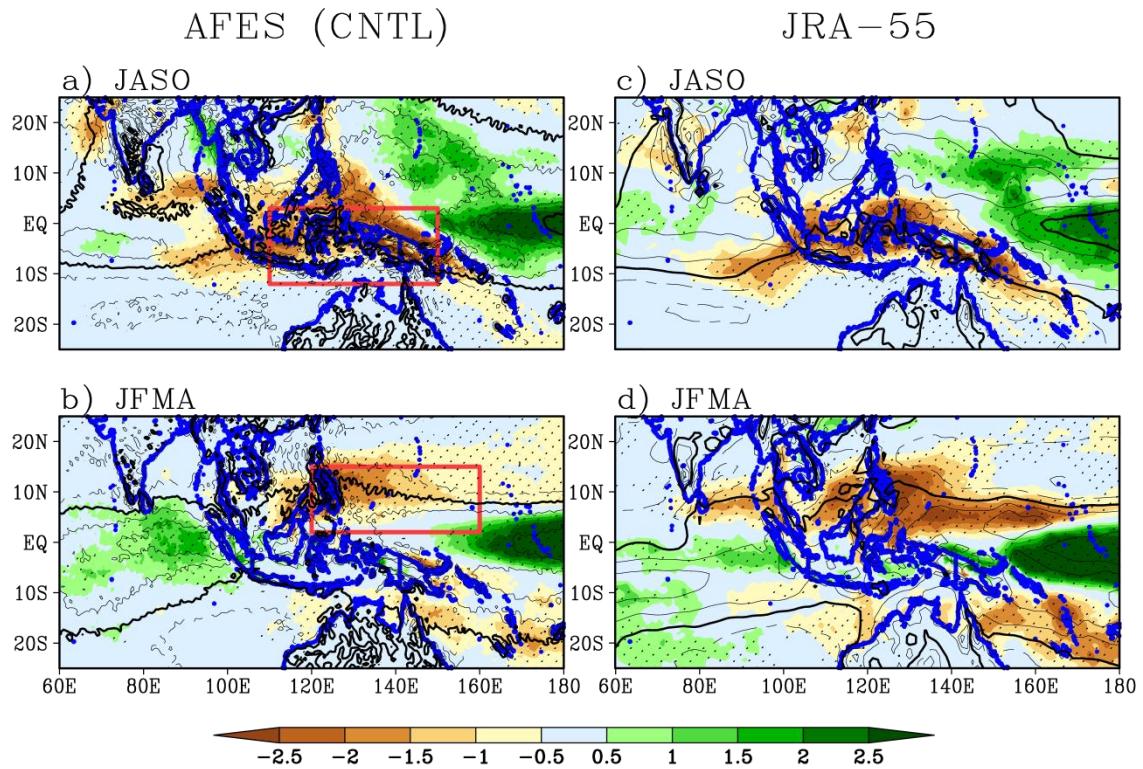
Fig. 3.3. Spatial distribution of anomalous precipitation (shading; mm day^{-1}) regressed against normalized Niño-3.4 index and climatological vertically integrated moisture flux convergence (contours; mm day^{-1}) for the JASO and JFMA seasons with use of the control (CNTL) run of the AFES model (left panels) and the JRA-55 reanalysis data (right panels). Dots denote the values that are significant at the 95% confidence level. The solid (dashed) contours shown are 3, 6, and 9 (-3, -6, and -9), and the thick contour is the zero contour. The red rectangular areas denote the regions for which the area-averaged precipitation is shown in Fig. 3.4.
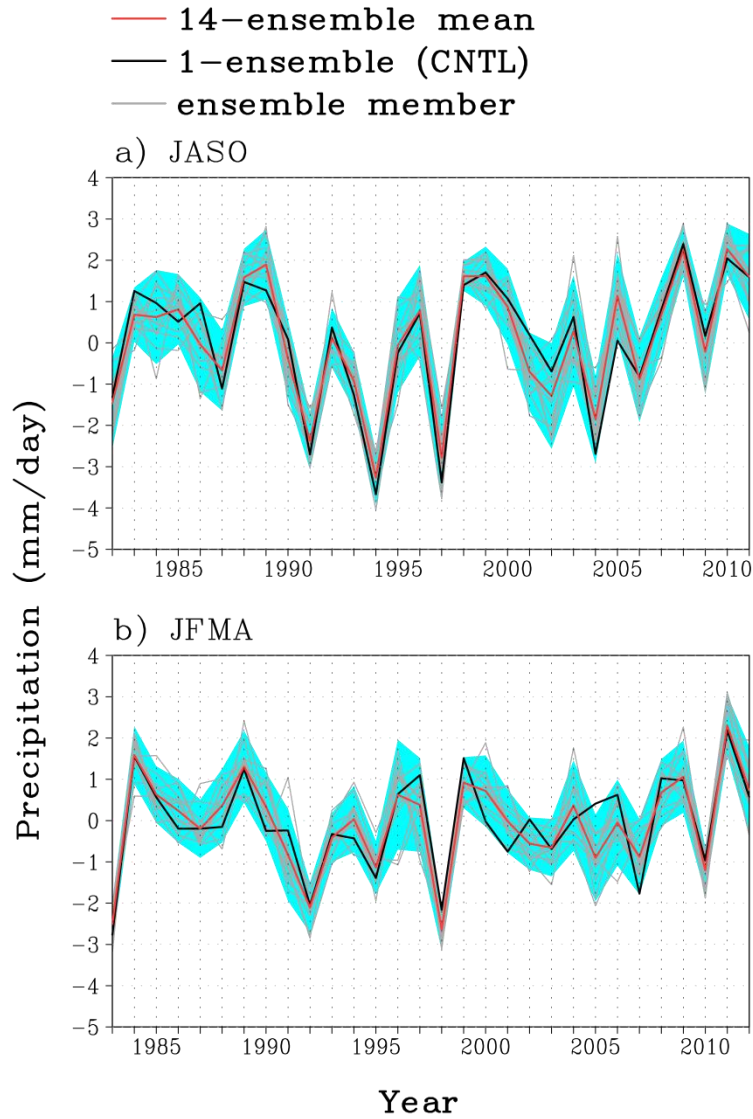
Fig. 3.4. Time series of precipitation (mm day^{-1}) for 14-ensemble mean (red), 1-ensemble as used for the CNTL run (black), and 13-ensemble member (gray) averaged over the area in Fig. 3.3, namely, (a) the southern hemisphere of MC (110°–150°E, 12°S–3°N) during the JASO season and (b) the northern hemisphere of MC (120°–160°E, 2°–15°N) during the JFMA season. Cyan shading denotes 5-95% confidence intervals.
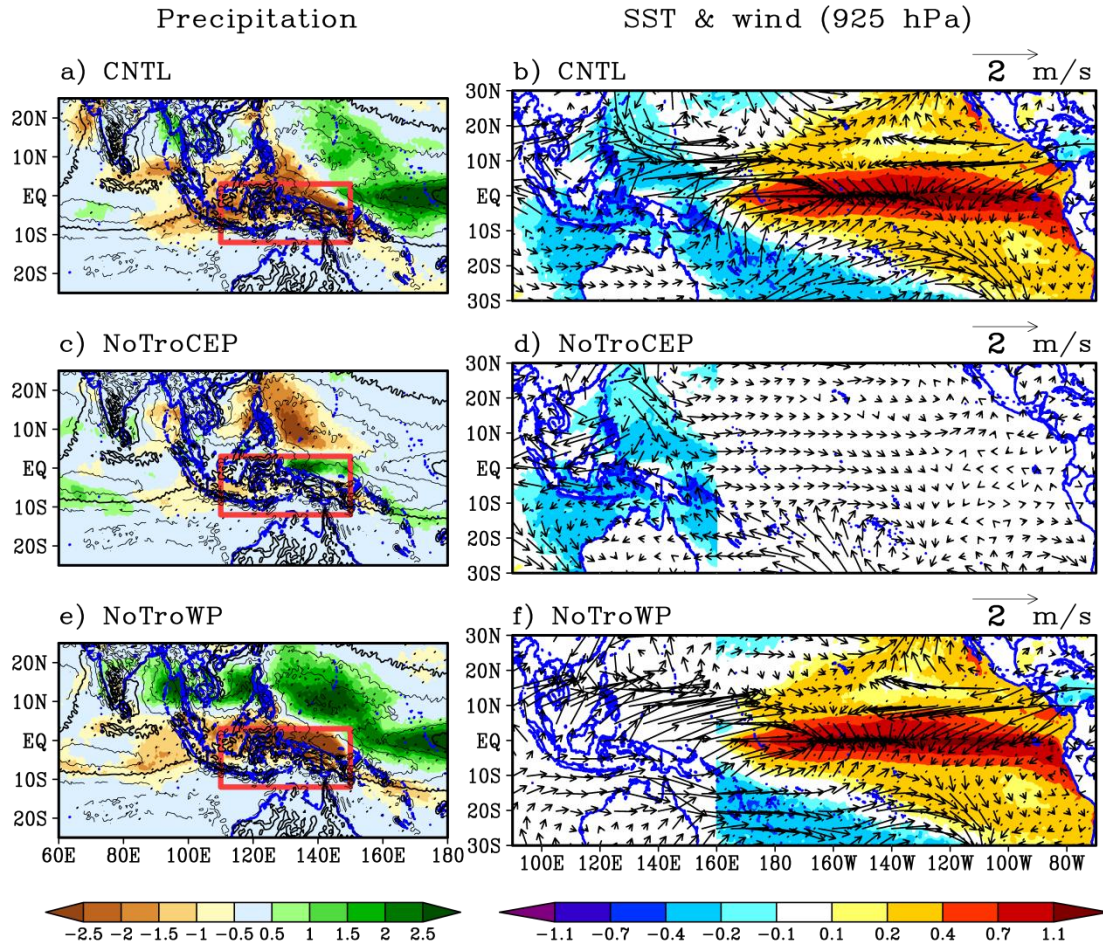
Fig. 3.5. (Left panels) spatial distribution of anomalous precipitation (shading; mm day⁻¹) regressed against normalized Niño-3.4 index and climatological vertically integrated moisture flux convergence (contours; mm day⁻¹) for the JASO season in (a) CNTL, (c) NoTroCEP, and (e) NoTroWP. (Right panels) spatial distribution of anomalous SST (shading; °C) and 925 hPa horizontal wind (vector) regressed against normalized Niño-3.4 index for the JASO season in (b) CNTL, (d) NoTroCEP, and (f) NoTroWP. Dots denote the values that are significant at the 95% confidence level. The solid (dashed) contours shown are 3, 6, and 9 (-3, -6, and -9), and the thick contour is the zero contour. The wind scale is given by the arrows at the top right corner. The red rectangular areas denote the regions for which the area-averaged precipitation is shown in Fig. 3.6.
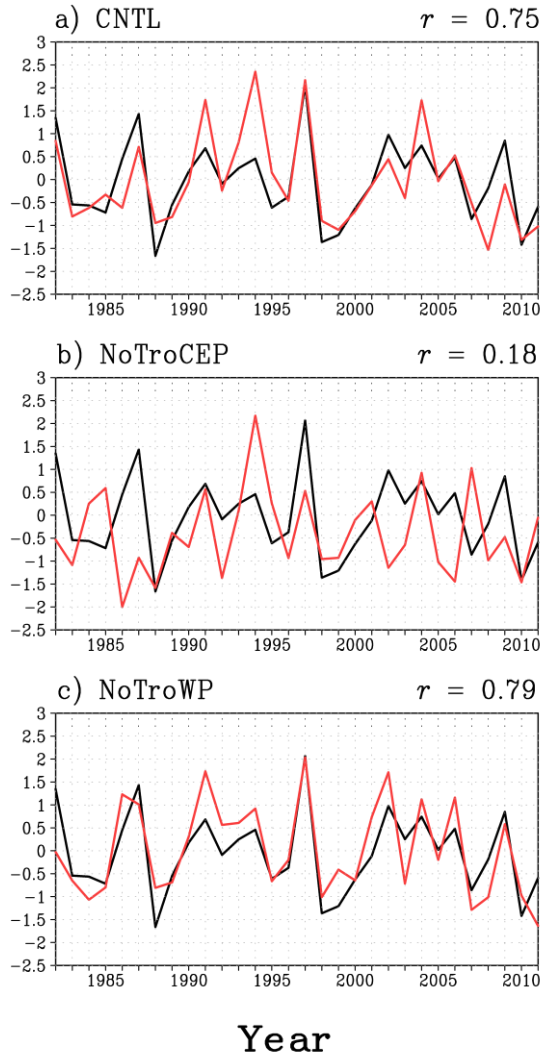
Normalized time series

Fig. 3.6. Time series of normalized Niño-3.4 index and normalized and sign-reversed precipitation averaged over the area in Fig. 3.5, namely, the southern hemisphere of MC (110°–150°E, 12°S–3°N) during the JASO season for (a) CNTL, (b) NoTroCEP, and (c) NoTroWP. The sign of precipitation is reversed for an easier comparison with Niño-3.4.
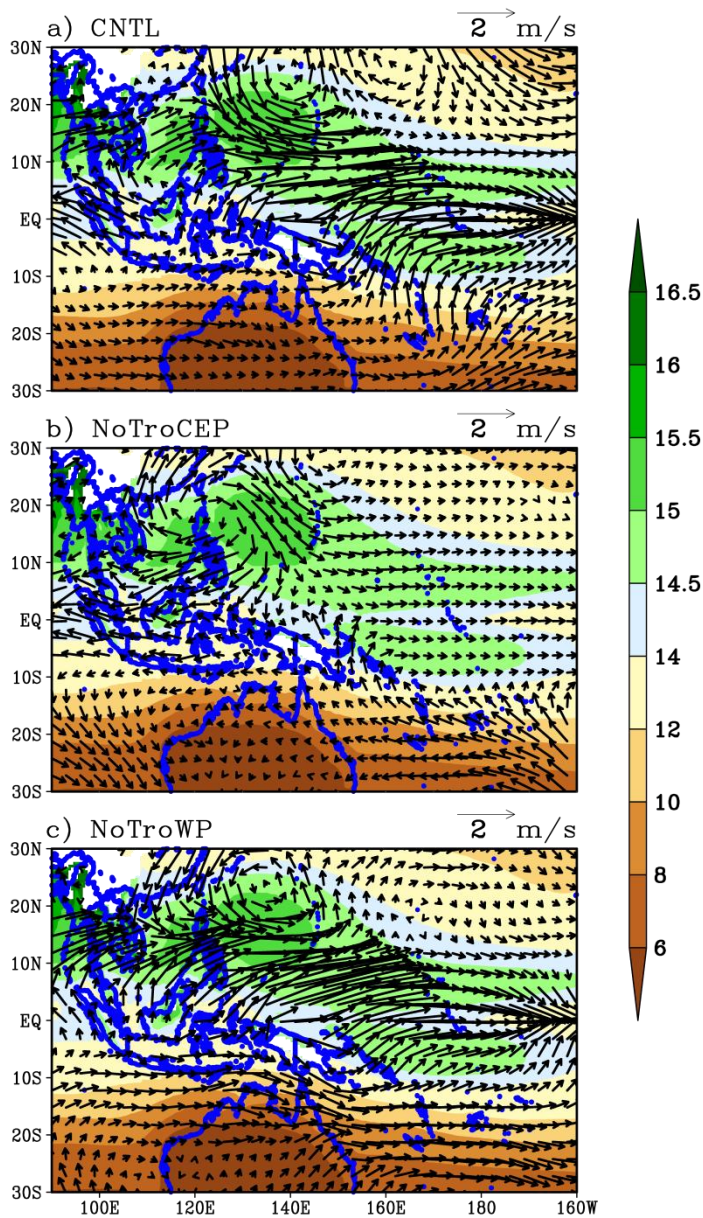
Fig. 3.7. JASO-mean 925 hPa climatological specific humidity (shading; g kg^{-1}) and anomalous horizontal wind (vector) regressed onto normalized Niño-3.4 index for (a) CNTL, (b) NoTroCEP, and (c) NoTroWP. The wind scale is given by the arrows at the top right corner.
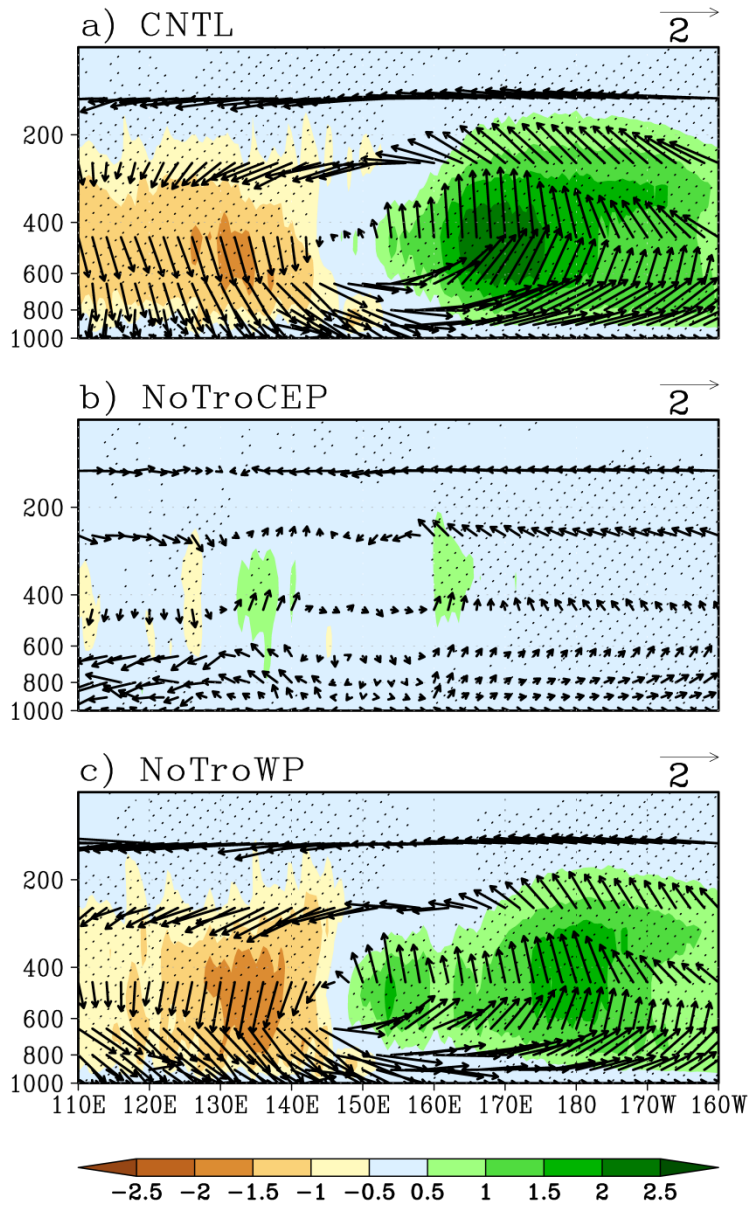
Fig. 3.8. Anomalous Walker circulation depicted by vectors consisting of the zonal wind anomaly (m s^{-1}) and p-vertical velocity anomaly (scaled by –0.01 Pa s^{-1}) regressed onto normalized Niño-3.4 index averaged between 15°S–5°N during JASO season for (a) CNTL, (b) NoTroCEP, and (c) NoTroWP. Positive and negative p-vertical velocity anomaly (shading) represents upward and downward motion, respectively. Dots denote the values of p-vertical velocity anomaly that are significant at the 95% confidence level.
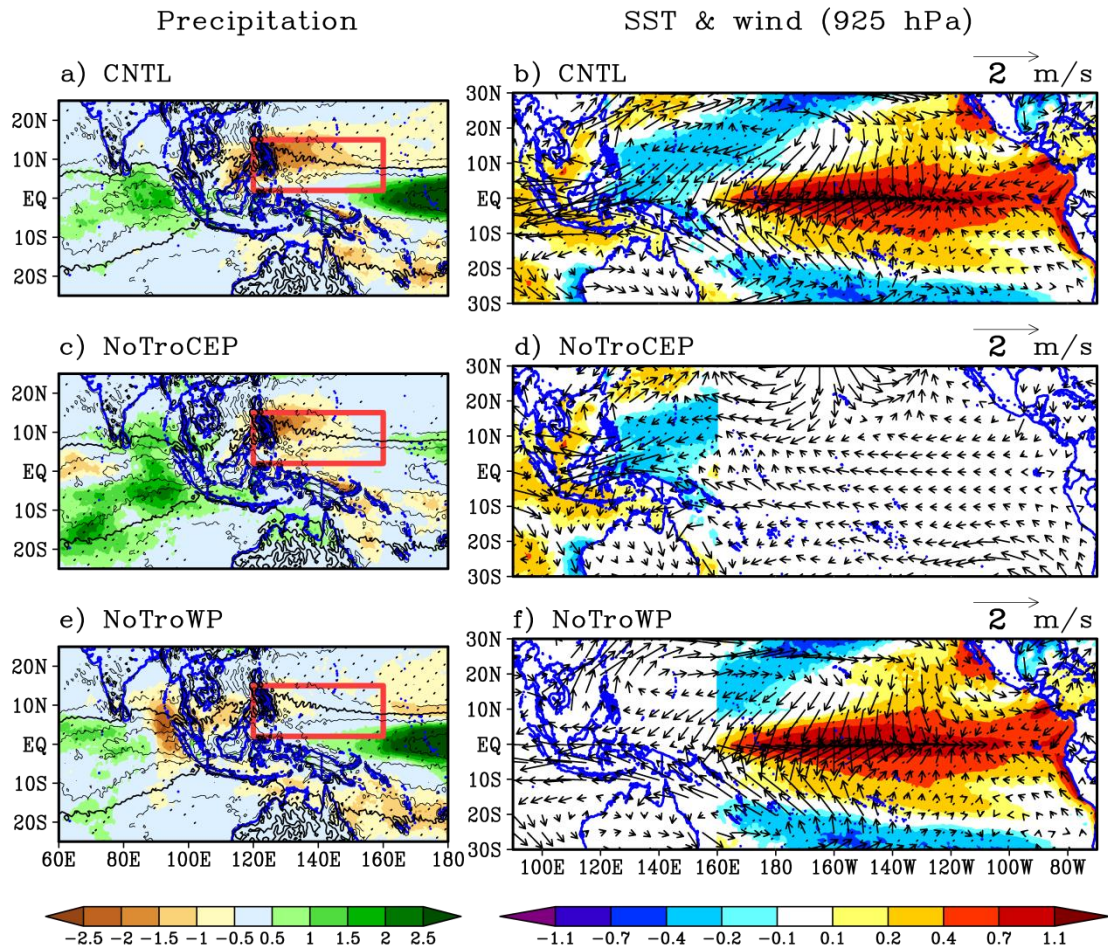
Fig. 3.9. As in Fig. 3.5, but for the JFMA season. The red rectangular areas denote the regions for which the area-averaged precipitation is shown in Fig. 3.10.
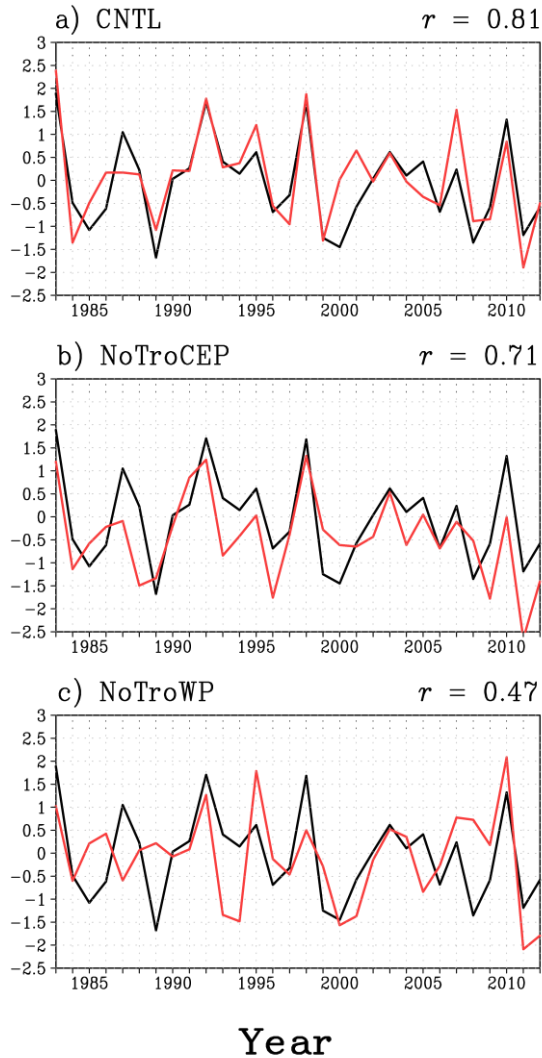
Fig. 3.10. Time series of normalized Niño-3.4 index and normalized and sign-reversed precipitation averaged over the area in Fig. 3.9, namely, the northern hemisphere of MC (120°–160°E, 2°–15°N) during the JFMA season for (a) CNTL, (b) NoTroCEP, and (c) NoTroWP. The sign of precipitation is reversed for an easier comparison with Niño-3.4.
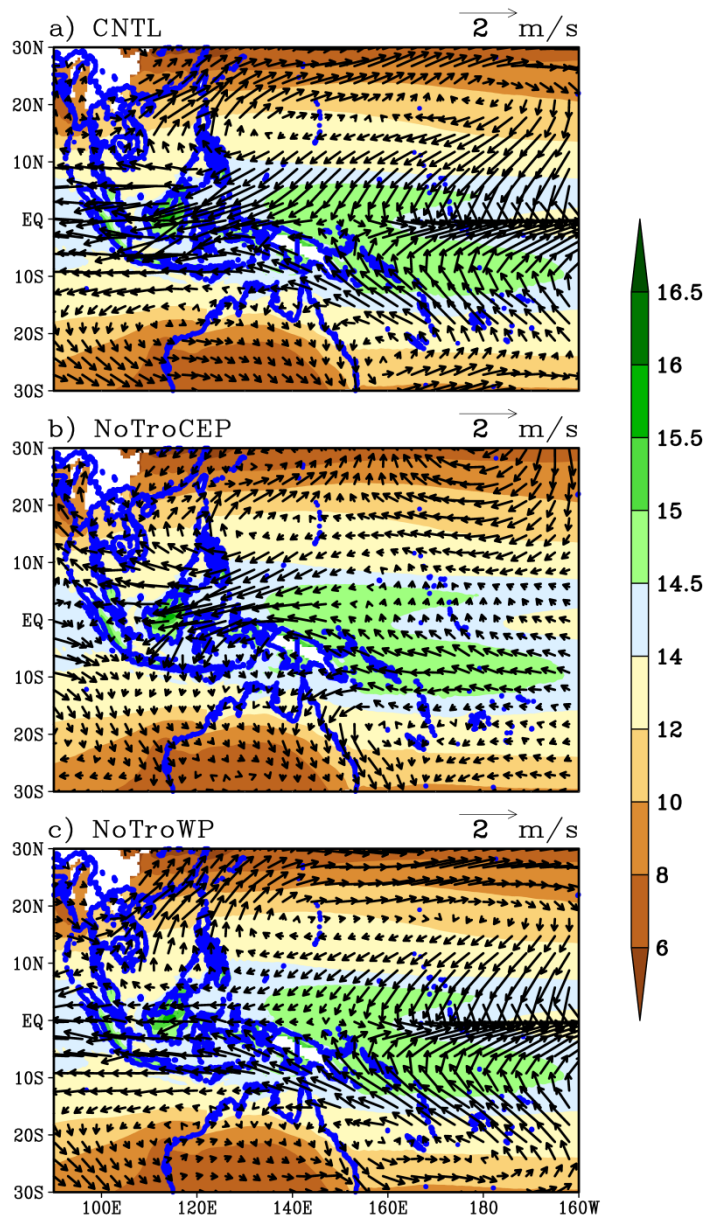
Fig. 3.11. As in Fig. 3.7, but for JFMA-mean.

Chapter 4

General Summary

The interannual variability of precipitation over the Maritime Continent (MC) related to El Niño is examined in this study. We used a gauge-based high-resolution precipitation APHRODITE dataset and performed numerical experiments using the AFES model. In this chapter, we summarize the major findings of chapters 2 and 3.

In chapter 2, the seasonal evolution of regional-scale Indonesian precipitation responses to El Niño is investigated. The influence of El Niño is not stationary across the country but exhibits seasonal migration. Significant precipitation reductions due to El Niño are found in central-eastern Indonesia during the dry season, and subsequently the precipitation reductions occur in a more limited area over northern Indonesia during the wet season. Corresponding to the decreased precipitation in the dry (wet) season anomalous divergence occurs around the southern (northern) edge of the convergence zones when one of the two edges reaches the equator (10°S–15°N), which is related to their seasonal migration. This mainly explains the seasonality and regionality of precipitation responses to El Niño.

In chapter 3, the relative role of remote and local SSTA forcing in shaping the interannual variations of large-scale precipitation over the Maritime Continent due to El Niño is investigated. The precipitation responses show strong seasonal dependency to El Niño. During the JASO season, precipitation reduction mainly occurs over the southern hemisphere side of MC, which is explained as a direct or remote influence of El Niño. Strong positive SSTA over the tropical CEP region generates off-equatorial twin Rossby wave cyclonic anomalies over the tropical WP. The southern branch of cyclonic anomalies advects dry air into the southern hemisphere side of MC, which suppresses convection and

precipitation there. In the JFMA season, the decreased precipitation is mainly confined over the northern hemisphere side of MC, and local SSTA forcing plays an important role. Eastern flank of the anticyclonic anomaly in the northern hemisphere induced by local SSTA forcing can advect dry air into the northern hemisphere side of MC and then can reduce local precipitation.

These findings are obviously important both for the application as well as for scientific purposes. The information provided by this study is essential for identifying the best policy options to mitigate the impacts of El Niño. For example, if El Niño is predicted, regions over the southern hemisphere of MC, especially central-eastern Indonesia, and over the northern hemisphere of MC should prepare for drought during the boreal summer-autumn and winter-spring, respectively. The present results can also be used as a hint in determining which climate models are appropriate for a study of future changes of El Niño-related precipitation anomalies over the MC region, by judging whether the responses of large-scale convergence zones to El Niño are realistic in those models. Furthermore, through numerical experiments, this study helps to reveal which SSTA forcing is the leading factor for the seasonal dependency precipitation responses over the MC to the El Niño events.

Acknowledgment

References

Adler, R. F., and Coauthors, 2003: The version 2 global precipitation climatology project (GPCP) monthly precipitation analysis (1979–present). *J. Hydrometeor.*, **4**, 1147–1167.

Aldrian, E., and R. D. Susanto, 2003: Identification of three dominant rainfall regions within Indonesia and their relationship to sea surface temperature. *Int. J. Climatol.*, **23**, 1425–1452.

Alsepan, G., and S. Minobe, 2020: Relations between interannual variability of regional-scale Indonesian precipitation and large-scale climate modes during 1960–2007. *J. Climate*, **33**, 5271–5291.

Amien, I., P. Redjakiningrum, B. Kartiwa, and W. Estiningtyas, 1999: Simulated rice yields as affected by interannual climate variability and possible climate change in Java. *Climate Res.*, **12**, 145–152.

An, S.-I., and F.-F. Jin, 2004: Nonlinearity and asymmetry of ENSO. *J. Climate*, **17**, 2399–2412.

Ashok, K., Z. Guan, and T. Yamagata, 2003: A look at the relationship between the ENSO and the Indian Ocean dipole. *J. Meteor. Soc. Japan*, **81**, 41–56.

Ashok, K., Z. Guan, and T. Yamagata, 2003: Influence of the Indian Ocean Dipole on the Australian winter rainfall. *Geophys. Res. Lett.*, **30**, 1821, doi:10.1029/2003GL017926.

Ashok, K., Z. Guan, N. H. Saji, and T. Yamagata, 2004: Individual and combined influences of ENSO and the Indian Ocean Dipole on the Indian summer monsoon. *J. Climate*, **17**, 3141–3155.

——, S. K. Behera, S. A. Rao, H. Weng, and T. Yamagata, 2007: El Niño Modoki and its possible teleconnection. *J. Geophys. Res.*, **112**, C11007, doi:10.1029/2006JC003798.

——, and N. H. Saji, 2007: On the impacts of ENSO and Indian Ocean dipole events on sub-regional Indian summer monsoon rainfall. *Nat. Hazards*, **42**, 273–285.

——, and T. Yamagata, 2009: The El Niño with a difference. *Nature*, **461**, 481–484.

As-syakur, A. R., and Coauthors, 2014: Observation of spatial patterns on the rainfall response to ENSO and IOD over Indonesia using TRMM Multisatellite Precipitation Analysis (TMPA). *Int. J. Climatol.*, **34**, 3825–3839.

Baba, Y., 2020: Shallow convective closure in a spectral cumulus parameterization. *Atmos. Res.*, **233**, 104707.

Bellenger, H., E. G. Guilyardi, J. Leloup, M. Lengaigne, and J. Vialard, 2014: ENSO representation in climate models: from CMIP3 to CMIP5. *Climate Dyn.*, **42**, 1999–2018.

Bjerkness, J., 1969: Atmospheric teleconnections from the equatorial Pacific. *Mon. Wea. Rev.*, **97**, 163–172.

Burgers, G., and D. B. Stephenson, 1999: The normality of El Niño. *Geophys. Res. Lett.*, **26**, 1027–1030.

Burton, C., R. A. Betts, C. D. Jones, T. R. Feldpausch, M. Cardoso, and L. O. Anderson, 2020: El Niño driven changes in global fire 2015/16. *Front. Earth Sci.*, **8**, 199.

Cai, W., T. Cowan, and M. Raupach, 2009: Positive Indian Ocean Dipole events precondition southeast Australia bushfires. *Geophys. Res. Lett.*, **36**, L19710, doi:10.1029/2009GL039902.

Chang, C-P, Z. Wang, J. Ju, and T. Li, 2004: On the relationship between western Maritime Continent monsoon rainfall and ENSO during northern winter. *J. Climate*, **17**, 665–672.

Chen, D., T. Lian, C. Fu, M. A. Cane, Y. Tang, R. Murtugudde, X. Song, Q. Wu, and L. Zhou, 2015: Strong influence of westerly wind bursts on El Niño diversity. *Nature Geoscience*, **8**, 339–345.

Chen, M., and T. Li, 2021: ENSO evolution asymmetry: EP versus CP El Niño. *Climate Dyn.*, **56**, 3569–3579.

——, X.-Y. Shen, and B. Wu, 2016: Relative roles of dynamic and thermodynamic processes in causing evolution asymmetry between El Niño and La Niña. *J. Climate.*, **29**, 2201–2220.

D'Arrigo, R., and R. Wilson, 2008: El Niño and Indian Ocean influences on Indonesian drought: implication for forecasting rainfall and crop productivity. *Int. J. Climatol.*, **28**, 611–616.

——, R. Allan, R. Wilson, J. Palmer, J. Sakulich, J. E. Smerdon, S. Bijaksana, and L. O. Ngkoimani, 2008: Pacific and Indian Ocean climate signals in a tree-ring record of Java monsoon drought. *Int. J. Climatol.*, **28**, 1889–1901.

Dai, A., K. E. Trenberth, and T. R. Karl, 1998: Global variations in droughts and wet spells: 1900–1995. *Geophys. Res. Lett.*, **25**, 3367–3370.

Delman, A. S., J. L. McClean, J. Sprintall, L. D. Talley, and F. O. Byan, 2018: Process-specific contributions to anomalous Java mixed layer cooling during positive IOD events. *J. Geophys. Res.*, **123**, 4153–4176.

Desser, C., M. A. Alexander, S.-P. Xie, and A. S. Phillips, 2010: Sea surface temperature variability: Patterns and mechanisms. *Annu. Rev. Mar. Sci.*, **2**, 115–143.

Ding, H., N. S. Keenlyside, and M. Latif, 2012: Impact of the equatorial Atlantic on the El Niño Southern Oscillation. *Climate Dyn.*, **38**, 1965–1972.

Doi, T., S. K. Behera, and T. Yamagata, 2016: Improved seasonal prediction using the SINTEX-F2 coupled model. *J. Adv. Model. Earth Syst.*, **8**, 1847–1867.

Emanuel, K. A., 1991: A scheme for representing cumulus convection in large-scale models. *J. Atmos. Sci.*, **48**, 2313–2335.

——, and M. Živković-Rothman, 1999: Development and evaluation of a convection scheme for use in climate models. *J. Atmos. Sci.*, **56**, 1766–1782.

Enomoto, T., A. Kuwano-Yoshida, N. Komori, and W. Ohfuchi, 2008: Description of AFES 2: Improvements for high-resolution and coupled simulations. *High Resolution Numerical Modeling of the Atmosphere and Ocean*, H. Kevin and O. Wataru, Eds., Springer, 77–97.

FAO, 2016: El Niño: Preparedness and response. *Situation Report March 2016*, retrieved on 14th June 2021 from http://www.fao.org/fileadmin/user_upload/emergencies/docs/1_FAO%20El%20Nino%20Sit%20Rep_March%202016.pdf.

Folland, C. K., J. A. Renwick, M. J. Salinger, and A. B. Mullan, 2002: Relative influences of the interdecadal Pacific oscillation and ENSO on the south Pacific convergence zone. *Geophys. Res. Lett.* **29**, 1643, doi:10.1029/2001GL014201.

Freitas, A. C. V., L. Aimola, T. Ambrizzi, and C. P. de Oliveira, 2017: Extreme intertropical convergence zone shifts over southern maritime continent. *Atmos. Sci. Lett.* **18**, 2–10.

Giannini, A., A. W. Robertson, and J-H. Qian, 2007: A role for tropical tropospheric temperature adjustments to El Niño–Southern Oscillation in the seasonality of monsoonal Indonesia precipitation predictability. *J. Geophys. Res.*, doi:10.1029/2007JD008519.

Gill, A. E., 1980: Some simple solutions for heat-induced tropical circulation. *Quart. J. Roy. Meteor. Soc.*, **106**, 447–462.

Good, P., R. Chadwick, C. E. Holloway, J. Kennedy, J. A. Lowe, R. Roehrig, and S. S. Rushley, 2020: High sensitivity of tropical precipitation to local sea-surface temperature. *Nature*, **589**, 408–414.

Guan, Z., K. Ashok, and T. Yamagata, 2003: Summertime response of the tropical atmosphere to the Indian Ocean Dipole sea surface temperature anomalies. *J. Meteor. Soc. Japan*, **81**, 533–561.

Gutman, G., I. Csiszar, and P. Romanov, 2000: Using NOAA/AVHRR products to monitor

El Niño impacts: focus on Indonesia in 1997–98. *Bull. Amer. Meteor. Soc.*, **81**, 1189–1205.

Haarsma, R. J., and Coauthors, 2016: High resolution model intercomparison project (HighResMIP v1.0) for CMIP6. *Geosci. Model. Dev.*, **9**, 4185–4208.

Hamada, A., O. Arakawa, and A. Yatagai, 2011: An automated quality control method for daily rain-gauge data. *Glob. Environ. Res.*, **15**, 165–172.

Hamada, J.-I., S. Mori, H. Kubota, M. D. Yamanaka, U. Haryoko, S. Lestari, R. Sulistyowati, and F. Syamsudin, 2012: Interannual rainfall variability over northwestern Jawa and its relation to the Indian Ocean Dipole and El Niño-Southern Oscillation events. *SOLA*, **8**, 69–72.

Harada, Y., H. Kamahori, C. Kobayashi, and H. Endo, 2016: The JRA-55 Reanalysis: representation of atmospheric circulation and climate variability. *J. Meteor. Soc. Japan*, **94**, 269–302.

Harris, I., P. D. Jones, T. J. Osborn, and D. H. Lister, 2014: Updated high-resolution grids of monthly climatic observations–the CRU TS3.10 dataset. *Int. J. Climatol.*, **34**, 623 – 642, doi:101002/joc.3711.

Haylock, M., and J. L. McBride, 2001: Spatial coherence and predictability of Indonesian wet season rainfall. *J. Climate*, **14**, 3882–3887.

Hendon, H. H., 2003: Indonesian rainfall variability: impacts of ENSO and local air-sea interaction. *J. Climate*, **16**, 1775–1790.

Hoerling, M. P., A. Kumar, and M. Zhong, 1997: El Niño, La Niña, and the nonlinearity of their teleconnections. *J. Climate*, **10**, 1769–1786.

Huffman, G. J., and Coauthors, 2007: The TRMM Multisatellite Precipitation Analysis (TMPA): quasi-global, multiyear, combined-sensor precipitation estimates at fine scales. *J. Hydrometeor.*, **8**, 38–55.

Hui, C., and X.-T. Zheng, 2018: Uncertainty in Indian Ocean Dipole response to global

warming: the role of internal variability. *Climate Dyn.*, **51**, 3597–3611.

Huijnen, V., and Coauthors, 2016: Fire carbon emissions over maritime Southeast Asia in 2015 largest since 1997. *Sci. Rep.*, **6**, 26886, doi:10.1038/srep26886.

Hung, C. W., X. Liu, and M. Yanai, 2004: Symmetry and asymmetry of the Asian and Australian summer monsoons. *J. Climate*, **17**, 2413–2426.

Iizumi, T., J.-J. Luo, A. J. Challinor, G. Sakurai, M. Yokozawa, H. Sakuma, M. E. Brown, and T. Yamagata, 2014: Impacts of El Niño Southern Oscillation on the global yields of major crops. *Nat. Commun.*, **5**, 3712.

Jia, X., J. Ge, S. Wang, 2016: Diverse impacts of ENSO on wintertime rainfall over the Maritime Continent: DIVERSE IMPACT OF ENSO. *Int. J. Climatol.*, **36**, 3384–3397.

Jiang, L., and T. Li, 2018: Why rainfall response to El Niño over Maritime Continent is weaker and non-uniform in boreal winter than in boreal summer. *Climate Dyn.*, **51**, 1465–1483.

Jin, F.-F., S.-I. An, A. Timmermann, and J. Zhao, 2003: Strong El Niño events and nonlinear dynamical heating. *Geophys. Res. Lett.*, doi:10.1029/2002GL016356.

Ju, J., and J. M. Slingo, 1995: The Asian summer monsoon and ENSO. *Quart. J. Roy. Meteor. Soc.*, **121**, 1133–1168.

Kalnay, E., and Coauthors, 1996: The NCEP/NCAR 40-year reanalysis project. *Bull. Amer. Meteor. Soc.*, **77**, 437–471.

Kang, L.-S., and J.-S. Kug, 2002: El Niño and La Niña sea surface temperature anomalies: Asymmetry characteristics associated with their wind stress anomalies. *J. Geophys. Res.*, doi:10.1029/2001JD000393.

Klein, S. A., B. J. Soden, and N-C. Lau, 1999: Remote sea surface temperature variations during ENSO: evidence for a tropical atmospheric bridge. *J. Climate*, **12**, 917–932.

Kobayashi, S., and Coauthors, 2015: The JRA-55 Reanalysis: general specifications and

basic characteristics. *J. Meteor. Soc. Japan*, **93**, 5–48.

Kodama, C., A. Kuwano-Yoshida, S. Watanabe, T. Doi, H. Kashimura, and T. Nasuno, 2019: JASMTEC model intercomparison project (JMIP). *JASMTEC Rep. Res. Dev.*, **28**, 5–34.

Kosaka, Y., and S.-P. Xie, 2016: The tropical Pacific as a key pacemaker of the variable rates of global warming. *Nature Geoscience*, **9**, 669–674.

Kucharski, F., A. Bracco, J. H. Yoo, and F. Molteni, 2007: Low-frequency variability of the Indian monsoon-ENSO relationship and the tropical Atlantic: the "weakening" of the 1980s and 1990s. *J. Climate*, **20**, 4255–4266.

Kuwano-Yoshida, A., T. Enomoto, and W. Ohfuchi, 2010: An improved PDF cloud scheme for climate simulations. *Quart. J. Roy. Meteor. Soc.*, **136**, 1583–1597.

——, ——, 2013: Predictability of explosive cyclogenesis over the Northwestern Pacific region using ensemble reanalysis. *Mon. Wea. Rev.*, **141**, 3769–3785.

——, S. Minobe, 2017: Strom-track response to SST fronts in the northwestern Pacific region in an AGCM. *J. Climate*, **30**, 1081–1102.

Lawrimore, J. H., and Coauthors, 2001: Climate assessment for 2000. *Bull. Amer. Meteor. Soc.*, **82**, S1–S55.

Lau, N.-C., and M. J. Nath, 2003: Atmosphere–ocean variations in the Indo–Pacific sector during ENSO episodes. *J. Climate*, **16**, 3–20.

Lee, T., and M. J. McPhaden, 2010: Increasing intensity of El Niño in the central-equatorial Pacific. *Geophys. Res. Lett.*, **37**, L14603, doi:10.1029/2010GL044007.

Lee, S-K., C. Wang, and B. E. Mapes, 2009: A simple atmospheric model of the local and teleconnection responses to tropical heating anomalies. *J. Climate*, **22**, 272–284.

Lestari, D. O., E. Sutriyono, Sabaruddin, and I. Iskandar, 2018: Respective influences of Indian Ocean Dipole and El Niño-Southern Oscillation on Indonesian

precipitation. *J. Math. Fund. Sci.*, **50**, 257–272.

Li, T., Y.-C. Tung, and J.-W. Hwu, 2005: Remote and local SST forcing in shaping Asian–Australian monsoon anomalies. *J. Meteor. Soc. Japan*, **83**, 153–167.

Liang, X.-Z., W.-C. Wang, and J. S. Boyle, 1997: Atmospheric ozone climatology for use in general circulation models. Retrieved on 14th June 2021 from https://pcmdi.llnl.gov/report/ab43.html.

Mantua, N. J., S. R. Hare, Y. Zhang, J. M. Wallace, and R. C. Francis, 1997: A Pacific interdecadal climate oscillation with impacts on salmon production. *Bull. Amer. Meteor. Soc.*, **78**, 1069–1079.

Matsuno, T., 1966: Quasi-geostrophic motions in the equatorial area. *J. Meteor. Soc. Japan*, **44**, 25–42.

Matthews, A. J., and G. N. Kiladis, 1999: Interactions between ENSO, transient circulation, and tropical convection over the Pacific. *J. Climate*, **12**, 3062–3086.

——, 2012: A multiscale framework for the origin and variability of the South Pacific Convergence Zone. *Quart. J. Roy. Meteor. Soc.*, **138**, 1165–1178.

McPhaden, M. J., 1999: Genesis and evolution of the 1997–1998 El Niño. *Science*, **283**, 950–954.

Meyers, G., O. McIntosh, L. Pigot, and M. Pook, 2007: The years of El Niño, La Niña, and interactions with the tropical Indian Ocean. *J. Climate*, **20**, 2872–2880.

Minobe, S., 1997: A 50–70 year climatic oscillation over the North Pacific and North America. *Geophys. Res. Let.*, **24**, 683–686.

——, A. Kuwano-Yoshida, N. Komori, S.-P. Xie, and R. J. Small, 2008: Influence of the Gulf Stream on the troposphere. *Nature*, **452**, 206–209.

Mishra, V., B. V. Smoliak, D. P. Lettenmaier, and J. M. Wallace, 2012: A prominent pattern of year-to-year variability in Indian summer monsoon rainfall. *Proc. Natl. Acad. Sci. USA*, **109**, 7213–7217.

Miyoshi, T., and S. Yamane, 2007: Local ensemble transform Kalman filtering with an

AGCM at a T159/L48 resolution. *Mon. Wea. Rev.*, **135**, 3841–3861.

——, ——, T. Enomoto, 2007: The AFES-LETKF experimental ensemble reanalysis: ALERA. *SOLA*, **3**, 45–48.

Nakanishi, M., and H. Niino, 2004: An improved Mellor-Yamada level-3 model with condensation physics: Its design and verification. *Boundary-Layer Meteorol.*, **112**, 1–31.

Naylor, R., W. Falcon, D. Rochberg, and N. Wada, 2001: Using El Niño/Southern Oscillation climate data to predict rice production in Indonesia. *Climatic Change*, **50**, 255–265.

Neale, R., and J. Slingo, 2003: The Maritime Continent and its role in the global climate: a GCM study. *J. Climate*, **16**, 834–848.

Ngo-duc, T., and Coauthors, 2017: Performance evaluation of RegCM4 in simulating extreme rainfall and temperature indices over the CORDEX-Southeast Asia region. *Int. J. Climatol.*, **37**, 1634–1647.

Noojipady, P., and Coauthors, 2017: Managing fire risk during drought: the influence of certification and El Niño on fire-driven forest conversion for oil palm in Southeast Asia. *Earth Sys. Dyn.*, **8**, 749–771.

Numaguti, A., M. Takahashi, T. Nakajima, and A. Sumi, 1997: Description of CCSR/NIES atmospheric general circulation model. *Study on the climate system and mass transport by a climate model, CGER's Supercomputer Monograph Report No. 3*, 1–48.

Nur'utami, M. N., and R. Hidayat, 2016: Influences of IOD and ENSO to Indonesian rainfall variability: role of atmosphere-ocean interaction in the Indo-Pacific sector. *Procedia Environ. Sci.*, **33**, 196–203.

Ogata, T., B. Taguchi, A. Yamamoto, and M. Nonaka, 2021: Potential predictability of the tropical cyclone frequency over the western north pacific with 50-km AGCM

ensemble experiments. *J. Geophys. Res. Atmos.*, **126**, e2020JD034206.

Ogawa, F., H. Nakamura, K. Nishii, T. Miyasaka, and A. Kuwano-Yoshida, 2012: Dependence of the climatological axial latitudes of the tropospheric westerlies and storm tracks on the latitude of an extratropical oceanic font. *Geophys. Res. Lett.*, **39**, doi:10.1029/2011GL049922.

Ohfuchi, W., and Coauthors, 2004: 10-km mesh meso-scale resolving simulations of the global atmosphere on the Earth Simulator–preliminary outcomes of AFES (AGCM for the Earth Simulator). *J. Earth Simul.* **1**, 8–34.

Okajima, S., H. Nakamura, K. Nishii, T. Miyasaka, A. Kuwano-Yoshida, B. Taguchi, M. Mori, and Y. Kosaka, 2018: Mechanisms for the maintenance of the wintertime basin-scale atmospheric response to decadal SST variability in the North Pacific subarctic frontal zone. *J. Climate*, **31**, 297–315.

Oouchi, K., J. Yoshimura, H. Yoshimura, R. Mizuta, S. Kusunoki, and A. Noda, 2006: Tropical cyclone climatology in a global-warming climate as simulated in a 20 km-mesh global atmospheric model: Frequency and wind intensity analyses. *J. Meteor. Soc. Japan*, **84**, 259–276.

Page, S. E., F. Siegert, J. O. Rieley, H. D. V. Boehm, A. Jaya, and S. Limin, 2002: The amount of carbon released from peat and forest fires in Indonesia during 1997. *Nature*, **420**, 61–65.

Palmer, T. M., and J. A. Owen, 1986: A possible relationship between some "severe" winters in North America and enhanced convective activity over the tropical west Pacific. *Mon. Wea. Rev.*, **114**, 648–651.

Pan, X., M. Chin, C. M. Ichoku, and R. D. Field, 2018: Connecting Indonesian fires and drought with the type of El Niño and phase of the Indian Ocean Dipole during 1979–2016. *J. Geophys. Res.*, **123**, 7974–7988.

Peng, M. S., J. A. Ridout, and T. F., Hogan, 2004: Recent modifications of the Emanuel

convective scheme in the navy operational global atmospheric prediction system. *Mon. Wea. Rev.*, **132**, 1254–1268.

Philander, S. G. H., 1983a: El Niño southern oscillation phenomena. *Nature*, **302**, 295–301.

——, 1983b: Anomalous El Niño of 1982–83. *Nature*, **305**, 16.

——, 1990: *El Niño, La Niña, and the Southern Oscillation*. Academic Press, 293 pp.

Preethi, B., T. P. Sabin, J. A. Adedoyin, and K. Ashok, 2015: Impacts of the ENSO Modoki and other tropical Indo-Pacific climate-drivers on African rainfall. *Sci. Rep.*, **5**, 16653, doi:10.1038/srep16653.

Qian, W., Y. Deng, Y. Zhu, and W Dong, 2002: Demarcating the worldwide monsoon. *Theor. Appl. Climatol.*, **71**, 1–16.

Qian, J. H., 2008: Why precipitation is mostly concentrated over islands in the Maritime Continent. *J. Atmos. Sci.*, **65**, 1428–1441.

Quinn, W., D. Zopf, K. Short, and R. Yang, 1978: Historical trends and statistics of the Southern Oscillation, El Niño, and Indonesian drought, *Fish. Bull.*, **76**, 663–678.

Ramage, C. S., 1968: Role of a tropical "Maritime Continent" in the atmospheric circulation. *Mon. Wea. Rev.*, **96**, 365–370.

Rasmusson, E. M., and T. H. Carpenter, 1982: Variations in tropical sea surface temperature and surface wind fields associated with the Southern Oscillation/ El Niño. *Mon. Wea. Rev.*, **110**, 354–384.

Ratnam, J. V., S. K. Behera, Y. Masumoto, and T. Yamagata, 2014: Remote effects of El Niño and Modoki events on the austral summer precipitation of southern Africa. *J. Climate*, **27**, 3802–3815.

Rayner, N. A., D. E. Parker, E. B. Horton, C. K. Folland, L. V. Alexander, D. P. Rowell, E. C. Kent, and A. Kaplan, 2003: Global analysis of sea surface temperature, sea ice, and night marine air temperature since the late nineteenth century. *J. Geophys.*

Res., **108**, 4407, doi:10.1029/2002JD002670.

Reynolds, R. W., T. M. Smith, C. Liu, D. B. Chelton, K. S. Casey, and M. G. Schlax, 2007: Daily high-resolution-blended analyses for sea surface temperature. *J. Climate*, **20**, 5473–5496.

Roberts, M. J., and Coauthors, 2018: The benefits of global high resolution for climate simulation: process understanding and the enabling of stakeholder decisions at the regional scale. *Bull. Amer. Meteor. Soc.*, **99**, 2341–2359.

Rodríguez-Fonseca, B., I. Polo, J. García-Serrano, T. Losada, E. Mohino, C. R. Mechoso, and F. Kucharski, 2009: Are Atlantic Niños enhancing Pacific ENSO events in recent decades?. *Geophys. Res. Lett.*, **36**, L20705, doi:10.1029/2009GL040048.

Ropelewski, C. F., and M. S. Halpert, 1987: Global and regional scale precipitation patterns associated with the El Niño-Southern Oscillation. *Mon. Wea. Rev.*, **115**, 1606–1626.

Saji, N. H., B. N. Goswani, P. N. Vinayachandran, T. Yamagata, 1999: A dipole mode in the tropical Indian Ocean. *Nature*, **401**, 360–363.

——, and T. Yamagata, 2003b: Possible impacts of Indian Ocean Dipole mode events on global climate. *Climate Res.*, **25**, 151–169.

——, S. P. Xie, and T. Yamagata, 2006: Tropical Indian Ocean variability in the IPCC twentieth-century climate simulations. *J. Climate*, **19**, 4397–4417.

Sato, K., J. Inoue, A. Yamazaki, J.-H. Kim, M. Maturilli, K. Dethloff, S. R. Hudson, and M. A. Granskog, 2017: Improved forecasts of winter weather extremes over midlatitudes with extra Arctic observations. *J. Geophys. Res. Oceans*, **122**, 775–787.

Schaake, J., 2004: Application of prism climatologies for hydrologic modeling and forecasting in the western U.S. *Proc. 18th Conf. on Hydrology*, Seattle, WA, Amer. Meteor. Soc., 5.3, http://ams.confex.com/ams/pdfpapers/72159.pdf.

Schneider, U., T. Fuchs, A. Meyer-Christoffer, and B. Rudolf, 2008: Global Precipitation analysis products of the GPCC. Global Precipitation Climatology Centre, DWD, 13 pp. [Available online at ftp://ftp.dwd.de/pub/data/gpcc/PDF/GPCC_intro_products_2008.pdf].

Sekiguchi, M., and T. Nakajima, 2008: A k-distribution-based radiation code and its computational optimization for an atmospheric general circulation model, *J. Quant. Spectrosc. Radiat. Transfr*, **109**, 2779–2793.

Siegert, F., G. Ruecker, A. Hinrichs, and A. A. Hoffmann, 2001: Increased damage from fires in logged forests during droughts caused by El Niño. *Nature*, **414**, 437–440.

Stuecker, M. F., F.-F. Jin, A. Timmermann, and S. McGregor, 2015: Combination mode dynamics of the anomalous northwest Pacific anticyclone. *J. Climate*, **28**, 1093–1111.

Su, H., J. D. Neelin, and C. Chou, 2001: Tropical teleconnection and local response to SST anomalies during the 1997–1998 El Niño. *J. Geophys. Res.*, **106**, 20025–20043.

Takata, K., S. Emori, and T. Watanabe, 2003: Development of the minimal advanced treatments of surface interaction and runoff. *Glob. Planet. Change*, **38**, 209–222.

Takemura, T., T. Nozawa, S. Emori, T. Y. Nakajima, and T. Nakajima, 2005: Simulation of climate response to aerosol direct and indirect effects with aerosol transport-radiation model. *J. Geophys. Res.*, **110**, D02202, doi:10.1029/2004JD005029.

Trenberth, K. E., G. W. Branstator, D. Karoly, A. Kumar, N.-C. Lau, and C. Ropelewski, 1998: Progress during TOGA in understanding and modeling global teleconnections associated with tropical sea surface temperature. *J. Geophys. Res.*, **103**, 14291–14324.

Villafuerte, M. Q., and J. Matsumoto, 2015: Significant influences of global mean temperature and ENSO on extreme rainfall in southeast Asia. *J. Climate*, **28**, 1905–1919.

Vinayachandran, P. N., J. Kurian, and C. P. Neema, 2007: Indian Ocean response to

anomalous conditions in 2006. *Geophys. Res. Lett.*, **34**, L15602, doi:10.1029/2007GL030194.

Vincent, D. G., 1994: The south Pacific convergence zone (SPCZ): A review. *Mon. Wea. Rev.*, **122**, 1949–1970.

Walker, G. T., 1923: Correlations in seasonal variations of weather. VIII, A further study of world weather. *Men. Indian Meteor. Dept.*, **24**, 75–131.

——, 1924: Correlations in seasonal variations of weather. VIII, A further study of world weather. *Men. Indian Meteor. Dept.*, **24**, 275–332.

Wallace, J. M., E. M. Rasmusson, T. P. Mitchell, V. E. Kousky, E. S. Sarachik, and H. von Storch, 1998: On the structure and evolution of ENSO-related climate variability in the tropical Pacific: lessons from TOGA, *J. Geophys. Res.*, **103**, 14241–14260.

Wang, B., R. Wu, and X. Fu, 2000: Pacific–east Asian teleconnection: How does ENSO affect east Asian Climate?. *J. Climate*, **13**, 1517–1536.

——, R. G. Wu, and T. Li, 2003: Atmosphere–warm ocean interaction and its impacts on Asian–Australian monsoon variation. *J. Climate*, **16**, 1195–1211.

——, I.-S. Kang, and J.-Y. Lee, 2004: Ensemble simulation of Asian–Australian monsoon variability by 11 AGCMs. *J. Climate*, **17**, 803–818.

Wang, C. H., S.-P. Xie, and Y. Kosaka, 2018: Indo-western Pacific climate variability: ENSO forcing and internal dynamics in a tropical Pacific pacemaker simulation. *J. Climate*, **31**, 10123–10139.

Waple, A. M., and J. H. Lawrimore, 2003: State of the climate in 2002. *Bull. Amer. Meteor. Soc.*, **84**, S1–S68.

Webster, P. J., V. O. Magaña, T. N. Palmer, R. A. Thomas, M. Yanai, and T. Yasunari, 1998: Monsoons: processes, predictability, and the prospects for prediction. *J. Geophys. Res.*, **103**, 14451–14510.

Weng, H., K. Ashok, S. K. Behera, S. A. Rao, and T. Yamagata, 2007: Impacts of recent El

Niño Modoki on dry/wet conditions in the Pacific rim during boreal summer. *Climate Dyn.*, **29**, 113–129.

——, S. K. Behera, and T. Yamagata, 2009: Anomalous winter climate conditions in the Pacific rim during recent El Niño Modoki and El Niño events. *Climate Dyn.*, **32**, 663–674.

Whetton, P., and I. Rutherfurd, 1994: Historical ENSO teleconnections in the eastern hemisphere. *Climatic Change*, **28**, 221–253.

Wu, B., T. Li, T. Zhou, 2010: Asymmetry of atmosphere circulation anomalies over the western north Pacific between El Niño and La Niña. *J. Climate*, **23**, 4807–4822.

——, T. Zhou, and T. Li, 2012: Two distinct modes of tropical Indian Ocean precipitation in boreal winter and their impacts on equatorial western Pacific. *J. Climate.*, **25**, 921–938.

——, 2017a: Atmospheric dynamics and thermodynamics processes driving the western north Pacific anomalous anticyclone during El Niño. Part I: Maintenance mechanisms. *J. Climate*, **30**, 9621–9635.

——, 2017b: Atmospheric dynamics and thermodynamics processes driving the western north Pacific anomalous anticyclone during El Niño. Part II: Formation processes. *J. Climate*, **30**, 9637–9650.

Wu, R., and B. P. Kirtman, 2005: Roles of Indian and Pacific Ocean air-sea coupling in tropical atmospheric variability. *Climate Dyn.*, **25**, 155–170.

——, 2006: Changes in spread and predictability associated with ENSO in an ensemble coupled CGM. *J. Climate*, **19**, 4378–4396.

Xie, P. P., and P. A. Arkin, 1997: Global precipitation: a 17-year monthly analysis based on gauge observations, satellite estimates and numerical model outputs. *Bull. Amer. Meteor. Soc.*, **78**, 2539–2558.

Xie, S-P., K. Hu, J. Hafner, H. Tokinaga, Y. Du, G. Huang, and T. Sampe, 2009: Indian

ocean capacitor effect on Indo–western Pacific climate during the summer following El Niño. *J. Climate*, **22**, 730–747.

——, Y. Kosaka, Y. Du, K. Hu, J. Chowdary, and G. Huang, 2016: Indo-western Pacific Ocean capacitor and coherent climate anomalies in post-ENSO summer: A review. *Adv. Atmos. Sci.*, **33**, 411–432.

——, and Z.-Q Zhou, 2017: Seasonal modulations of El Niño–related atmospheric variability: Indo–western Pacific ocean feedback. *J. Climate*, **30**, 3461–3472.

Xu, Q., Z. Guan, D. Jin, and D. Hu, 2019: Regional characteristics of interannual variability of summer rainfall in the Maritime Continent and their related anomalous circulation patters. *J. Climate*, **32**, 4179–4192.

Yamagata, T., S. K . Behera, J. J. Luo, S. Masson, M. R. Jury, and S. A. Rao, 2004: Coupled ocean-atmosphere variability in the tropical Indian Ocean. *Geophys. Monogr. Ser.*, **147**, 189–211.

Yang, J., Q. Liu, S-P. Xie, Z. Liu, and L. Wu, 2007: Impact of the Indian ocean SST basin wide mode on the Asian summer monsoon. *Geophys. Res. Lett.*, **34**, L02708, doi:10.1029/2006GL028571.

Yanto, B. Rajagopalan, and E. Zagona, 2016: Space-time variability of Indonesian rainfall at inter-annual and multi-decadal time scales. *Climate Dyn.*, **47**, 2975–2989.

Yatagai, A., P. Xie, and A. Kitoh, 2005: Utilization of a new gauge-based daily precipitation dataset over monsoon Asia for validation of the daily precipitation climatology simulated by the MRI/JMA 20-km-mesh AGCM. *SOLA*, **1**, 193–196.

——, O. Arakawa, K. Kamiguchi, H. Kawamoto, M. I. Nodzu, and A. Hamada, 2009: A 44-year daily gridded precipitation dataset for Asia based on a dense network of rain gauges. *SOLA*, **5**, 137–140.

——, K. Kamiguchi, O. Arakawa, A. Hamada, N. Yasutomi, and A. Kitoh, 2012: APHRODITE: constructing a long-term daily gridded precipitation dataset for

Asia based on a dense network on rain gauges. *Bull. Amer. Meteor. Soc.*, **93**, 1401–1415.

——, T. N. Krishnamurti, V. Kumar, A. K. Mishra, and A. Simon, 2014: Use of APHRODITE rain gauge-based precipitation and TRMM 3B43 products for improving Asian monsoon seasonal precipitation forecasts by the superensemble method. *J. Climate*, **27**, 1062–1069.

Yeh, S. W., J. S. Kug, B. Dewitte, M. H. Kwon, B. P. Kirtman, and F. F. Jin, 2009: El Niño in a changing climate. *Nature*, **461**, 511–514.

Yoshioka, M. K., Y. Kurihara, and W. Ohfuchi, 2005: Effect of the thermal tidal oscillation of the atmosphere on tropical cyclones. *Geophys. Res. Lett.*, **32**, L16802.

——, ——, 2008: Influence of the equatorial warm water pool on the tropical cyclogenesis: an aqua planet experiment. *Atmos. Sci. Lett.*, **9**, 248–254.

Zhang, T., S. Yang, X. Jiang, and B. Huang, 2016: Roles of remote and local forcings in the variation and prediction of regional Maritime Continent rainfall in wet and dry seasons. *J. Climate*, **29**, 8871–8879.

Zebiak, S. E., 1993: Air-sea interaction in the equatorial Atlantic region. *J. Climate*, **6**, 1567–1586.